

# ReQISC: A Reconfigurable Quantum Computer Microarchitecture and Compiler Co-Design

Zhaohui Yang<sup>1</sup>, Dawei Ding<sup>2</sup>, Qi Ye<sup>3</sup>, Cupjin Huang<sup>4</sup>, Jianxin Chen<sup>5\*</sup>, Yuan Xie<sup>1</sup>

<sup>1</sup> The Hong Kong University of Science and Technology, Hong Kong

<sup>2</sup> Yau Mathematical Sciences Center, Tsinghua University, Beijing 100084, China

<sup>3</sup> Institute for Interdisciplinary Information Sciences, Tsinghua University, Beijing 100084, China

<sup>4</sup> DAMO Quantum Laboratory, Alibaba Group, Bellevue, WA 98004, USA

<sup>5</sup> Department of Computer Science and Technology, Tsinghua University, Beijing 100084, China

## Abstract

Despite remarkable milestones in quantum computing, the performance of current quantum hardware remains limited. One critical path to higher performance is to expand the quantum ISA with basis gates that have higher fidelity and greater synthesis capabilities than the standard CNOT. However, this substantially increases gate calibration overhead and introduces challenges in compiler optimization. Consequently, although more expressive ISAs (even complex, continuous gate sets) have been proposed, they are still primarily proof-of-concept and have not been widely adopted.

To move beyond these hurdles and unlock the performance gains offered by expressive continuous ISAs, we introduce the concept of “reconfigurable quantum instruction set computers” (ReQISC), which incorporates: (1) a unified microarchitecture capable of directly implementing arbitrary 2Q gates equivalently, i.e.,  $SU(4)$  modulo 1Q rotations, with theoretically optimal gate durations given any 2Q coupling Hamiltonians; (2) a compilation framework tailored to ReQISC primitives for end-to-end synthesis and optimization, comprising a program-aware pass that refines high-level representations, a program-agnostic pass for aggressive circuit-level optimization, and an  $SU(4)$ -aware routing pass that minimizes hardware mapping overhead.

We detail the hardware implementation to demonstrate the feasibility, in terms of both pulse control and calibration of this superior gate scheme on realistic hardware. By leveraging the expressivity of  $SU(4)$  and the time minimality realized by the underlying microarchitecture, the  $SU(4)$ -based ISA achieves remarkable performance, with a 4.97-fold reduction in average pulse duration to implement arbitrary 2Q gates, compared to the usual CNOT/CZ scheme on mainstream flux-tunable transmons. Supported by the end-to-end compiler, ReQISC outperforms the conventional CNOT-ISA, SOTA compiler, and pulse implementation counterparts, in significantly reducing 2Q gate counts, circuit depth, pulse duration, qubit mapping overhead, and program fidelity losses. For the first time, ReQISC makes the theoretical benefits of continuous ISAs practically feasible.

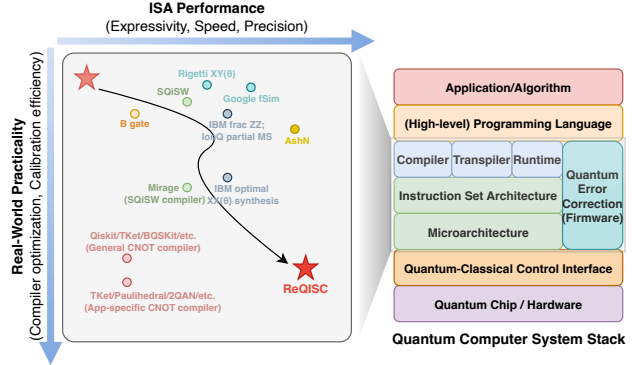


Figure 1. Advancing architectural support for quantum advantage.

## 1 Introduction

Quantum hardware has advanced rapidly over the past two decades, achieving milestones including quantum supremacy [3], quantum utility [35], and going below the fault-tolerant threshold [2]. Today’s quantum processors come with detailed device specifications such as native gate sets and pulse-level controls, accessible through a cloud interface or a complete system delivery. However, hardware noise presents critical challenges for both noisy intermediate-scale quantum (NISQ) [53] and fault-tolerant application-scale quantum (FASQ) [54] devices, significantly limiting executable program scales and impacting computational reliability [2, 3, 35].

To pursue a practical quantum advantage, many sophisticated architectural supports have been proposed by exploring advanced instruction set architectures (ISA) beyond the conventional CNOT-based paradigm (Figure 1). For specific applications, novel 2Q quantum gates like Google’s Sycamore from the fSim family offer higher fidelity and difficulty to simulate classically [3], while gates like SQiSW aim to improve fidelity and synthesis efficiency [29]. Physical platforms developed by Google, Rigetti, IonQ, Quantinuum, and IBM have also demonstrated continuous gate sets [1, 24, 30, 31, 55], which appear to yield improvements in fidelity [47, 64]. At the frontier, recent works have proposed using the entire  $SU(4)$  group as the most expressive ISA, achieving optimal-duration gates on flux-tunable transmons with 99.37% average fidelity in experiments [11, 14].

\* Corresponding author: chenjianxin@tsinghua.edu.cn.

Adopting more expressive quantum ISAs offers significant theoretical benefits, most notably a reduction in the 2Q gate count required for circuit synthesis [1, 11, 24, 30, 31]. This is demonstrated by comparing the Haar-random synthesis cost of representative 2Q basis gates against the standard CNOT-equivalent gates. For instance, the cost is 3 for CNOT/CZ/iSWAP [56], around 2.21 for SQiSW [29], 2 for B gate [72], and even lower for combinatorial or continuous gate sets [52]. However, despite the variety of quantum ISAs available, none have successfully usurped the dominance of the CNOT-based ISA due to several inherent challenges:

**Hardware implementation and calibration.** Implementing versatile 2Q gates with high precision and simple control via unified gate schemes across diverse quantum platforms remains a significant challenge, especially for complex, continuous quantum ISAs. For example, although B gate was proposed decades ago [72], it was only recently natively implemented [14, 48]; IBM’s fractional ZZ gates are deployed on their Heron QPUs [30], but they have the same gate time as CZ and on average 1.5 times the error rate of CZ, according to public data from IBM Quantum Platform [30]. Furthermore, each 2Q gate must be carefully and periodically calibrated to ensure high precision. While proposals exist to mitigate calibration overhead [33], their effectiveness is not guaranteed. Thus, a program with numerous distinct 2Q gates is hard to execute in practice.

**Compilation strategy.** Although the capability to implement more complex ISAs has been demonstrated, effectively utilizing them to compile programs into fewer gates with reduced circuit depth remains largely unaddressed. Neither gate set transpilation [45, 51, 67] nor numerically optimal synthesis [32, 38] effectively exploits their synthesis potential for real-world program compilation. We observe that ISA-customized strategies are crucial at every compilation stage, from high-level synthesis to hardware mapping. Otherwise, a theoretically superior ISA may be inferior in practice [32].

To overcome these challenges and establish the practical superiority of expressive continuous ISAs, we introduce ReQISC (Reconfigurable Quantum Instruction Set Computers). ReQISC is a full-stack framework that integrates compilation, ISA design, and pulse control to boost performance across versatile quantum hardware. At its core, ReQISC utilizes the most expressive  $SU(4)$  as its ISA (i.e., all 2Q gates) and makes it the most performant with minimal gate time through our proposed microarchitecture (gate scheme). The ReQISC microarchitecture can *straightforwardly implement arbitrary 2Q gates up to local equivalence in optimal time, via simple pulse controls, on any 2Q coupling Hamiltonian*. Recent experimental progress has affirmed the viability of specific mechanisms in this direction [14]; our scheme, however, represents a more generalized approach with extensive architectural exploration, extending the advantages to a broader spectrum of hardware. Our key contributions are as follows:

- ① We introduce a unified microarchitecture for native, time-optimal realization for all of  $SU(4)$  with arbitrary coupling Hamiltonians. We validate the pulse-control simplicity and calibration feasibility on representative hardware.
- ② We overcome the difficulty of implementing near-identity 2Q gates [11], by replacing them with their mirrors [16] and subsequently altering qubit mapping at compile time, ensuring no extra 2Q gate count overhead.
- ③ We present the first end-to-end compiler tailored to  $SU(4)$  characteristics. Based on the lower-bound analysis of required  $SU(4)$  resource for synthesizing multi-qubit circuits, our compiler employs both program-aware and program-agnostic passes to optimize the overall  $SU(4)$  gate count. We address the program-specific calibration overhead and also effectively manage the trade-off between calibration overhead and aggressive 2Q gate count reduction.
- ④ We propose the program-aware template-based synthesis method that first pre-synthesizes optimal  $SU(4)$ -based circuit templates for refined intermediate representations (IR) and then selectively assembles the whole circuit.
- ⑤ We also propose a hierarchical, program-agnostic synthesis pass to aggressively lower the 2Q gate count, building on circuit partitioning and approximate synthesis. We introduce the partitioning compactness metric to guide co-optimization and develop a directed acyclic graph (DAG) compacting pass based on approximate commutation rules in our findings.
- ⑥ Furthermore, we introduce a novel  $SU(4)$ -aware routing pass, dubbed mirroring-SABRE, which significantly reduces the routing overhead engendered by topology constraints.

## 2 Background

### 2.1 Quantum instruction set

Similar to its classical counterpart, a quantum ISA serves as an interface between software and hardware, by mapping high-level semantics of quantum programs to low-level native quantum operations or pulse sequences on hardware. Quantum instructions involve physical operations on qubits that alter their states. Typically, these instructions include qubit initialization, a universal gate set, and measurement. The universal gate set is the key component of a quantum ISA that dominates its hardware-implementation accuracy and cost, as well as the software expressivity. It is well known that a gate set consisting of any 2Q entangling gate (e.g., CNOT, iSWAP) together with all possible 1Q gates can achieve universal computation [9]. Instructions from a universal gate set correspond to dynamics governed by the system Hamiltonian  $H$ , potentially influenced by external drives. The evolution of a quantum state over time  $t$  is described by the unitary operator  $U(t) = e^{-iHt}$  which realizes the desired quantum gate up to a global phase.

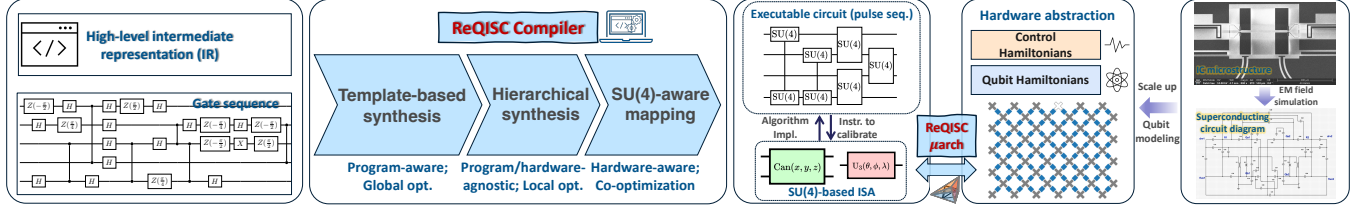


**Figure 2.** ReQISC workflow. It incorporates (1) the most performant (time-optimal realization) microarchitecture to engineer any arbitrary SU(4) gates given the hardware coupling Hamiltonian and (2) an end-to-end compilation framework with three-stage optimization passes to generate executable SU(4)-based circuits. The SU(4) ISA is expressed as the  $\{\text{Can}, U_3\}$  gate set.

## 2.2 Canonical decomposition and the Weyl chamber

The group  $SU(2^n)$  is a real manifold with dimension  $4^n - 1$ , each of which corresponds to an  $n$ -qubit unitary. A generic 2Q gate within  $SU(4)$ , despite having 15 real parameters, can have its nonlocal behavior fully characterized by only 3 real parameters. This method, known as Canonical decomposition or KAK decomposition from Lie algebra theory, is widely adopted in quantum computing [10, 61, 71, 75].

For any  $U \in SU(4)$ , there exists a unique vector  $\vec{\eta} = (x, y, z) \in W \subseteq \mathbb{R}^3$ , along with  $V_1, V_2, V_3, V_4 \in SU(2)$  and a global phase, such that

$$U = g \cdot (V_1 \otimes V_2) e^{-i\vec{\eta} \cdot \vec{\Sigma}} (V_3 \otimes V_4), \quad g \in \{1, i\}$$

where  $\vec{\Sigma} \equiv (XX, YY, ZZ)$  [61]. The set

$$W := \{(x, y, z) \in \mathbb{R}^3 \mid \pi/4 \geq x \geq y \geq |z|, z \geq 0 \text{ if } x = \pi/4\}$$

is known as the *Weyl chamber* [71], and  $\vec{\eta} \in W$  is known as the *Weyl coordinate* of  $U$ . We also refer to a gate of the form  $\text{Can}(x, y, z) := e^{-i\vec{\eta} \cdot \vec{\Sigma}}$  as a *canonical* gate. Two 2Q gates  $U$  and  $V$  are considered *locally equivalent* if they differ only by 1Q gates. For example,  $\text{CNOT} \sim \text{CZ}$ , as  $\text{CZ} = (I \otimes H) \text{CNOT} (I \otimes H)$  and their canonical coordinates are both  $(\pi/4, 0, 0)$ .

## 3 Our Proposal: ReQISC

Figure 2 illustrates the overall workflow of ReQISC. The end-to-end ReQISC compiler first converts quantum programs in high-level IR or gate sequences in conventional (e.g., CNOT-based) ISAs into SU(4) operations, as depicted by the circuit composed of  $\text{Can}(x, y, z)$  and  $U_3(\theta, \phi, \lambda)$  gates. Subsequently, a set of simple pulse control parameters for desired SU(4) instructions is computed via the ReQISC microarchitecture and calibrated before executing on hardware. Note that we do not alter the hardware at any step. The electromagnetic simulation and qubit modeling follow standard procedures to specify a 2Q coupling Hamiltonian and tunable 1Q drive Hamiltonians by adjusting control parameters.

## 4 The ReQISC microarchitecture

While any 2Q gate within the Weyl chamber can theoretically be realized through Hamiltonian steering [40, 46, 73], pulse concatenation or optimization [25, 50, 58], these methods often require complex control sequences or fail to achieve

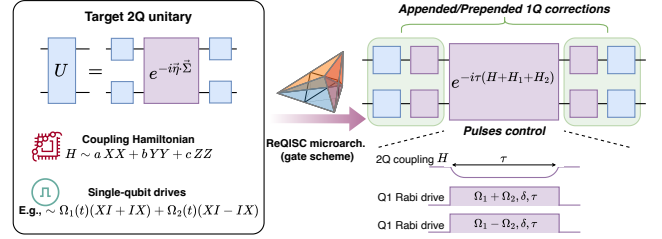


**Figure 3.** The ReQISC microarchitecture (gate scheme) directly implements arbitrary 2Q gates in a unified control. Common 2Q coupling form and standard 1Q Rabi drives with control parameters  $\Omega_1, \Omega_2, \delta, \tau$ , are sufficient to generate an evolution locally equivalent to the target unitary  $U$ . With the additional 1Q corrections appended/prepended to the solved evolution  $e^{-i\tau(H+H_1+H_2)}$ , the circuit in the right figure exactly implements  $U$ .

time-optimal gate implementation. In contrast, we propose a unified, straightforward, and unequivocally superior control scheme that directly implements (up to local equivalence) arbitrary 2Q gates in optimal time, as depicted by Figure 3 and Algorithm 1. Inspired by the AshN gate scheme [11] which was limited to  $XX + YY$  coupling, our scheme accommodates arbitrary coupling Hamiltonians for any quantum processor, whether it be superconducting, trapped-ion, or other platforms, significantly broadening applicability. Time optimality [28] refers to the theoretical lower bound of evolution time to achieve an equivalent 2Q unitary given the coupling Hamiltonian, with tunable parallel local drives. This is essential for minimizing the qubits' exposure to decoherence and also for reducing overall runtime.

### 4.1 Protocol design (Hamiltonian description)

To illustrate the general applicability of our scheme, we consider the most general 2Q coupling Hamiltonian and local Rabi drives [73] for a pair of resonant qubits ( $\omega_{q_1} = \omega_{q_2} = \omega$ ), with experimentally tunable pulse parameters:

$$H = aXX + bYY + cZZ; H_{d_i} = -\frac{1}{2}A_i(t)X_i + \delta Z \quad (1)$$

where  $(a, b, c)$  are the canonical coupling coefficients [8] with  $a \geq b \geq |c|$ . We define the coupling strength  $g := a + b + |c|$ . For flux-tunable superconducting qubits, in the drive frame

**Algorithm 1:** ReQISC Microarchitecture Design

---

**Input :** Coupling Hamiltonian  $H \in \mathcal{H}(\mathbb{C}^{4 \times 4})$ ; Target  $U \in \text{SU}(4)$   
**Output:** 2Q gate time  $\tau$ ; Local Hamiltonians  $H_1, H_2 \in \mathcal{H}(\mathbb{C}^{2 \times 2})$ ;  
 1Q gate corrections  $A_1, A_2, B_1, B_2 \in \text{SU}(2)$

```

1   $(x, y, z, A'_1, A'_2, B'_1, B'_2) \leftarrow \text{CANONICALDECOMPOSE}(U)$ ;
2   $(a, b, c, H'_1, H'_2, U_1, U_2) \leftarrow \text{NORMALFORM}(H)$ ;
3   $\tau_0, \tau_+, \tau_- \leftarrow \frac{x}{a}, \frac{x+y-z}{a+b-c}, \frac{x+y+z}{a+b+c}; \tau_1 \leftarrow \max\{\tau_0, \tau_+, \tau_-\}$ ;
4   $\tau'_0, \tau'_+, \tau'_- \leftarrow \frac{\frac{x}{a}-x}{a}, \frac{\frac{x}{a}-x+y+z}{a+b-c}, \frac{\frac{x}{a}-x+y-z}{a+b+c}; \tau_2 \leftarrow \max\{\tau'_0, \tau'_+, \tau'_-\}$ ;
5   $\tau \leftarrow \min\{\tau_1, \tau_2\}$ ;
6  if  $\tau_2 < \tau_1$  then
7     $x \leftarrow \frac{\pi}{2} - x; z \leftarrow -z; \tau_0, \tau_+, \tau_- \leftarrow \tau'_0, \tau'_+, \tau'_-;$ 
8  end
9  if  $\tau = \tau_0$  then
10    $S_1 \leftarrow \text{sinc}^{-1}\left(\frac{\sin(y-z)}{(b-c)\tau}\right)/\tau$  where  $S_1 \geq b - c$ ;
11    $S_2 \leftarrow \text{sinc}^{-1}\left(\frac{\sin(y+z)}{(b+c)\tau}\right)/\tau$  where  $S_2 \geq b + c$ ;
12    $\Omega_1 \leftarrow \frac{1}{2}\sqrt{S_1^2 - (b-c)^2}; \Omega_2 \leftarrow \frac{1}{2}\sqrt{S_2^2 - (b+c)^2}; \delta \leftarrow 0$ ;
13 else
14    $\text{lhs}(\alpha, \beta, \eta, t) := \frac{(1-\alpha)(1+\alpha+\beta)-(1-\alpha+\beta)\eta}{(1-\alpha+\beta)(1-\eta+\alpha+2\beta)} e^{-i(2+2\beta-\eta)t} +$ 
      $\frac{\beta(1+\alpha+\beta)-(1-\alpha+\beta)\eta}{(1-\alpha+\beta)(2\alpha+\beta-\eta)} e^{i(\eta-2\alpha)t} +$ 
      $\frac{(1+\alpha-\eta)\eta-\beta(1-\alpha-\eta)}{(2\alpha+\beta-\eta)(1+\alpha+2\beta-\eta)} e^{i(2\alpha+2\beta-\eta)t};$ 
15    $\text{rhs}(x, y, z) := e^{i(x-y-z)} - e^{i(y-x-z)} + e^{i(z-x-y)}$ ;
16   if  $\tau = \tau_+$  then
17      $x', y', z' \leftarrow x + c\tau, y + c\tau, c\tau - z$ ;
18      $\eta \leftarrow (a-b)/(a+c); t \leftarrow (a+c)\tau$ ;
19      $(\alpha, \beta) \leftarrow \text{NSOLVE}(\text{lhs}(\alpha, \beta, \eta, t) = \text{rhs}(x', y', z'))$ 
     where  $(\alpha, \beta) \in [0, 1] \times [0, \infty)$  and  $\alpha + \beta \geq \eta$ ;
20      $\Omega_1 \leftarrow 0; \Omega_2 \leftarrow (a+c)\sqrt{(1-\alpha)\beta(1-\eta+\alpha+\beta)}$ ;
21      $\delta \leftarrow -(a+c)\sqrt{\alpha(1+\beta)(\alpha+\beta-\eta)}$ ;
22   else
23      $x', y', z' \leftarrow x - c\tau, y - c\tau, z - c\tau$ ;
24      $\eta \leftarrow (a-b)/(a-c); t \leftarrow (a-c)\tau$ ;
25      $(\alpha, \beta) \leftarrow \text{NSOLVE}(\text{lhs}(\alpha, \beta, \eta, t) = \text{rhs}(x', y', z'))$ 
     where  $(\alpha, \beta) \in [0, 1] \times [0, \infty)$  and  $\alpha + \beta \geq \eta$ ;
26      $\Omega_1 \leftarrow (a-c)\sqrt{(1-\alpha)\beta(1-\eta+\alpha+\beta)}; \Omega_2 \leftarrow 0$ ;
27      $\delta \leftarrow (a-c)\sqrt{\alpha(1+\beta)(\alpha+\beta-\eta)}$ ;
28   end
29 end
30  $H'_1, H'_2 \leftarrow (\Omega_1 + \Omega_2)X + \delta Z, (\Omega_1 - \Omega_2)X + \delta Z$ ;
31  $(x', y', z', A''_1, A''_2, B''_1, B''_2) \leftarrow$ 
    $\text{CANONICALDECOMPOSE}(e^{-i(aXX+bYY+cZZ+H'_1+H'_2)\tau})$ ;
    $/\ast (x', y', z') = (x, y, z) \ast /$ 
32  $H_1, H_2 \leftarrow U_1 H''_1 U_1^\dagger - H'_1, U_2 H''_2 U_2^\dagger - H'_2$ ;
33  $A_1, A_2 \leftarrow A'_1 (A''_1)^\dagger U_1^\dagger, A'_2 (A''_2)^\dagger U_2^\dagger$ ;
34  $B_1, B_2 \leftarrow U_1 (B''_1)^\dagger B'_1, U_2 (B''_2)^\dagger B'_2$ ;
    $/\ast (A_1 \otimes A_2) e^{-i\tau(H+H_1 \otimes I + I \otimes H_2)} (B_1 \otimes B_2) = U \ast /$ 

```

---

after the rotating wave approximation,  $a = b = g/2, c = 0, A_i$  is the amplitude of a square wave envelope for a sinusoidal drive and  $\delta_i := \frac{1}{2}(\omega_{d_i} - \omega)$  is the drive detuning. We actually show that it is sufficient to set the drive frequencies to be the same, so  $\delta_1 = \delta_2 = \delta$ . For other physical platforms,  $H_{d_1}$  and  $H_{d_2}$  may be realized via other means (e.g., lasers in Rydberg atoms or trapped ions). In this case,  $A_i$  and  $\delta_i$  may correspond to other physical parameters. Our framework can also be

easily adapted to other possible  $H_{d_1}, H_{d_2}$  (for example  $YI$  and  $IY$ ). By defining the symmetric and anti-symmetric combinations of drive amplitudes (for mathematical convenience)  $\Omega_{1,2} = -\frac{1}{4}(A_1 \pm A_2)$ , we can rewrite the local drives as

$$H_1 = (\Omega_1 + \Omega_2)XI + \delta ZI, H_2 = (\Omega_1 - \Omega_2)IX + \delta IZ. \quad (2)$$

The local drive amplitudes  $\Omega_1$  and  $\Omega_2$ , detuning  $\delta$ , and interaction duration  $\tau$  constitute the set of simple control parameters to be determined via our microarchitecture such that simultaneously applying  $H_1, H_2$  with the device 2Q coupling  $H$  for duration  $\tau$  implements a gate locally equivalent to a target gate  $U$ , as illustrated in Figure 3.

Algorithm 1 describes the details of our gate scheme. A target gate  $U$  and the device 2Q Hamiltonian  $H$  are provided as inputs. The goal is to determine the local Hamiltonians  $H_1$  and  $H_2$ , with the interaction duration  $\tau$ , such that  $e^{-i\tau(H+H_1+H_2)} \sim U$ . Specifically, the Weyl coordinates  $(x, y, z)$  of  $U$  are obtained via canonical decomposition (line 1), while the interaction Hamiltonian  $H$ , if not already in its native normalized form, is transformed into its normal form [21] to obtain its canonical coefficients  $(a, b, c)$  (line 2). The parameters  $(x, y, z)$  and  $(a, b, c)$  are then fed to the subsequent solving procedure that computes  $H_1, H_2, \tau$ . With additional 1Q gate corrections  $A_{1,2}$  and  $B_{1,2}$  (line 33 and 34),  $(A_1 \otimes A_2)e^{-i\tau(H+H_1 \otimes I + I \otimes H_2)}(B_1 \otimes B_2)$  exactly implements  $U$ .

Herein we give some intuition for Algorithm 1 while leaving the detailed proof in Appendix A. First, the interaction time  $\tau$  is determined as the maximum value among  $\{\tau_0, \tau_+, \tau_-\}$ . Which of the three is largest dictates the subscheme used: (1)  $\tau_0$ , that is, no-detuning (ND,  $\delta = 0$ ); (2)  $\tau_+$  for equal-amplitudes with opposite signs (EA<sub>+</sub>,  $\Omega_1 = 0$ ); (3)  $\tau_-$  for equal-amplitudes with same sign (EA<sub>-</sub>,  $\Omega_2 = 0$ ). The three subschemes correspond to three distinct regions that partition the Weyl chamber [11]. This partitioning of the Weyl chamber is convenient in terms of physical implementation but not unique. Each subscheme<sup>1</sup> involves transcendental equations to calculate amplitudes and/or detuning, which lacks analytical solutions and must be solved numerically. We can also prove Algorithm 1 provides a time-optimal [21, 28] realization for any 2Q gates in Appendix A.

## 4.2 Addressing the “near-identity” issue

Following Algorithm 1, we find that realizing gates with Weyl coordinate close to the identity gate (common in QFT and Hamiltonian simulation kernels) in optimal time requires unbounded pulse amplitudes, which are experimentally infeasible. While trading gate time for bounded amplitudes is possible [11], it leads to a more error-prone implementation due to longer duration and complex control. To address

<sup>1</sup>Note that  $\text{sinc}(x)$  (line 10 and 11) is not invertible (bijective), so  $S_1$  can correspond to any of the preimages. However, in hardware implementations, we typically select the smallest possible value to minimize the required pulse amplitude. Similarly, we opt for the smallest possible values when solving the equations in lines 19 and 25.

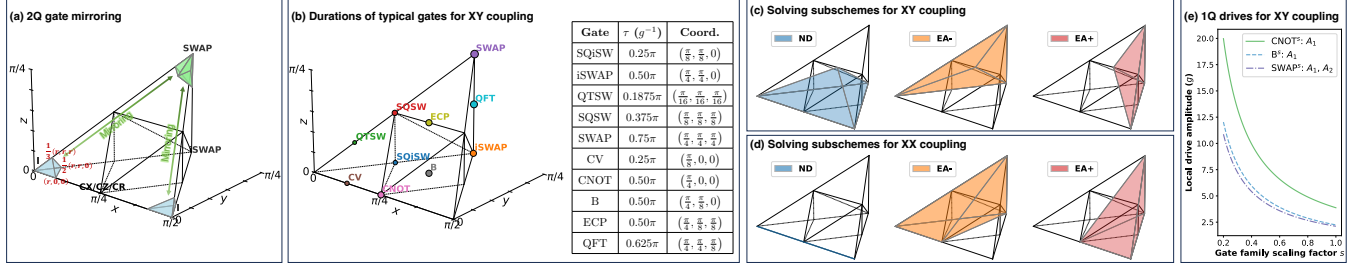


**Figure 4.** Hardware implementation of the ReQISC microarchitecture. (a) 2Q gate mirroring. The near-identity corner with a  $\mathcal{L}^1$  coordinate norm bounded by  $r$  is mirrored to the corner near SWAP. (b) Gate time landscape, computed under the XY coupling Hamiltonian  $H = \frac{g}{2}(XX + YY)$ , where the circle size indicates the corresponding gate duration within the Weyl chamber. (c-d): Pulse control subschemes, under XY and XX couplings, respectively. (e) Local drive amplitudes required for representative gate families. The scaling factor  $s$  represents the specific equivalent canonical gate within the gate family, e.g.,  $B^s \sim \text{Can}(s\frac{\pi}{4}, s\frac{\pi}{8}, 0)$ . iSWAP family requires no local drives so it is not shown in the figure; CNOT family and B family require only one-side drive ( $A_1 \neq 0$ ); SWAP family requires both-side drives ( $A_1, A_2 \neq 0$ ). Frequency-related quantities ( $A_1, A_2, \delta$ ) are normalized by the coupling strength  $g$ .

this, we propose transforming the near-identity gate into its mirror symmetry [16] differing by a SWAP gate, as

$$\text{SWAP} \cdot \text{Can}(x, y, z) \sim \begin{cases} \text{Can}(\frac{\pi}{4} - z, \frac{\pi}{4} - y, x - \frac{\pi}{4}), & \text{if } z \geq 0 \\ \text{Can}(\frac{\pi}{4} + z, \frac{\pi}{4} - y, \frac{\pi}{4} - x), & \text{if } z < 0 \end{cases}.$$

Thus the mirrors of near-identity gates are located far away from the identity, which is illustrated in Figure 4 (a). In the compilation stage, we appended the SWAP to each near-identity 2Q gate, leaving the circuit rewiring effects of these SWAPs to be resolved at compile time. Specifically, we define a coordinate norm threshold to determine if a 2Q gate is near-identity and requires mirroring. The threshold  $r$  in general depends on hardware parameters [11]. The impacts of inserted SWAPs are tracked by recording the altered qubit mappings, which are then used to rewire the entire circuit at the final step. Thus we resolve the issue at compile time without introducing additional #2Q overhead.

### 4.3 Hardware implementation

To implement our presented microarchitecture on any quantum platforms, the only requirement is that  $H_1, H_2$  can be applied simultaneously with the 2Q interaction. In the case of flux-tunable superconducting qubits, requirements for the control equipment are the same as that of typical experiments, i.e., standard microwave drives, AWGs, and mixers are sufficient, as recently validated experimentally [14]. Given these minimal requirements, many platforms, e.g., flux-tunable transmons [2, 3], fluxonium qubits [4, 49], Floquet qubits [48], semiconductor spin qubits [20], trapped ions [66], and some neutral-atom devices [7] could immediately benefit from this scheme. Herein we highlight its broad applicability via case studies and give the detailed pulse-control description.

We give examples to realize some commonly encountered 2Q gates (CNOT, iSWAP, B, etc.) with two typical coupling types—XY coupling ( $H = \frac{g}{2}(XX + YY)$ ) and XX coupling ( $H = gXX$ ). For instance, the former is a common form of

coupling in flux-tunable superconducting qubits [3, 37]; the latter is the dominant coupling type for trapped ions [66]. The latter type of coupling can also appear in capacitively coupled flux-tunable superconducting qubits by simply working in the lab frame instead of the drive frame [37]:

$$H = -\frac{\omega_1}{2}ZI - \frac{\omega_2}{2}IZ + gYY + V_1(t)YI + V_2(t)IY, \quad (3)$$

where  $\omega_i$  are the frequencies of the qubits,  $g$  is the coupling strength, and  $V_i(t)$  are the local drives. By conjugation by a local unitary, we can transform this to

$$H' = -\frac{\omega_1}{2}ZI - \frac{\omega_2}{2}IZ + gXX + V_1(t)XI + V_2(t)IX, \quad (4)$$

which falls under our framework. We can simply tune different qubit frequencies to control the  $ZI, IZ$  terms while local drives can be square pulses with variable amplitudes instead of sinusoidal pulses to control the  $XI, IX$  terms. This Hamiltonian example is explicitly not covered by [11] but can appear in hardware devices. Our gate scheme can handle this along with any other coupling Hamiltonian.

Through Algorithm 1, we can derive the subschemes (ND, EA<sub>+</sub>, or EA<sub>-</sub>) and control parameters for different situations, as shown in Figure 4 (c-e). By means of our scheme, some takeaways for ISA design are worth noting. For example, gates requiring no or weak local drives (low amplitude) potentially achieve higher fidelities than those requiring stronger drives (e.g., CNOT under XX coupling v.s. CNOT under XY coupling, iSWAP under XY coupling v.s. iSWAP under XX coupling), since precise calibration of local drives with the coupling turned on is nontrivial in practice. Using our gate scheme, SWAP is far less expensive than the conventional three-CNOT decomposition, as shown for XY coupling in Figure 4 (b). Even the CNOT implementation via our scheme is 1.41x faster than the traditional control scheme [37], that is,  $\pi/2g$  v.s.  $\pi/\sqrt{2}g$ . This speedup is critical for suppressing errors on platforms where decoherence is the dominant error source. Besides, our scheme does not



introduce the additional  $|11\rangle \leftrightarrow |02\rangle$  transition, thereby minimizing leakage error and dynamic stray ZZ crosstalk. Part of these features have been validated in superconducting transmon qubits by Chen et al. [14], where versatile 2Q gates are implemented in high fidelity (on average 99.37%), with optimal gate duration and simple pulse control. As our scheme represents a generalized approach to directly implement arbitrary SU(4) on physical platforms with other coupling Hamiltonians, it poses more opportunities for hardware-native ISA design and compiler optimization.

#### 4.4 Gate calibration

Gate calibration can follow a similar procedure as outlined in [14], where XY coupling is assumed. First, the iSWAP-family component of the Hamiltonian (coupling term  $H$ ) and the drive components ( $H_1$  and  $H_2$ ) are separately calibrated to determine how the model parameters  $g$ ,  $\Omega_{1,2}$ , and  $\delta$  depend on physical control parameters. This provides an initial estimate for physical control parameters. Then, the two parts of the Hamiltonian are simultaneously applied. Further optimization is achieved by first applying quantum process tomography [27]. This is used to measure the Weyl coordinate of the physical gate realized. Control parameters are tuned to minimize the Euclidean distance from target coordinates. Further fine tuning of the parameters can be achieved via cross-entropy benchmarking [3].

Such a calibration method is readily generalizable. For example, instead of calibrating an iSWAP-family gate, one would calibrate an  $XX(\theta)$  rotation for the case of XX coupling. To calibrate a continuous gate set, the idea in [11] could be utilized. In this case, we can calibrate the *mapping* between the control parameters and model parameters. Such a mapping can be expressed as some parameterized mathematical function. We can then optimize the parameters of this function via fully randomized benchmarking (Haar-random 2Q gates) [36] or other more general benchmarking schemes [12] with respect to different gate distributions.

## 5 ReQISC Compilation Framework

Using the ReQISC microarchitecture, we can natively realize the SU(4)-based ISA with theoretically optimal performance. However, a dedicated compiler is still required to fully unlock its potential, as compiling generic programs into 2Q basis gates is non-trivial. In this section, we delve into the ReQISC compiler design, which draws upon novel insights regarding the analysis of hardware primitives, the characteristics of quantum programs, and hardware requirements.

### 5.1 Local optimization: Hierarchical synthesis

We first attempt to exploit SU(4)’s synthesis potential based on its resource-bound analysis and work out a *hierarchical synthesis* structure to perform aggressive local optimization at the circuit level. We introduce a “compactness” metric

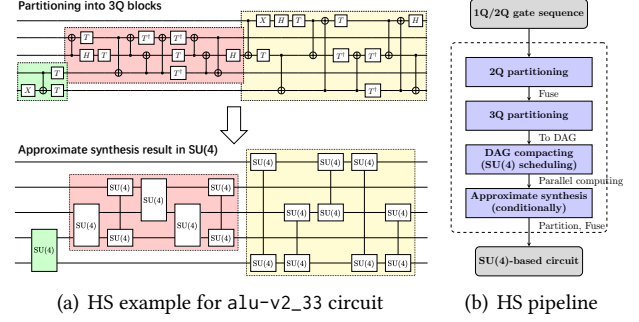


**Figure 5.** Example and pipeline of hierarchical synthesis (HS). (a) The original `alu-v2_33` circuit is partitioned into 3 three-qubit blocks with #2Q equal to 1, 8, and 8. After approximate synthesis on the latter two blocks, each has 5 SU(4)s. The overall #2Q is reduced from 17 to 11. (b) HS involves two-tier partitioning, followed by DAG compacting and conditional approximate synthesis.

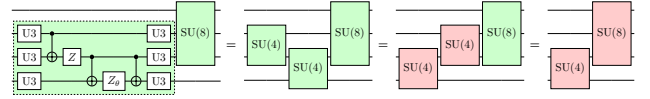


**Figure 6.** Exchanging two “approximately commutative” SU(4)’s improves compactness. This pattern occurs in `grover_5_0`. Different colors indicate that the parameters of SU(4) or SU(8) have changed.

across local subcircuits to guide co-optimization and devise a supporting *DAG compacting* pass with the *approximate commutation* rules in our findings.

**5.1.1 Resource analysis and approximate synthesis with SU(4).** The lower bound of 2Q basis gate count given a quantum ISA typically reflects its intrinsic synthesis power. The bound for an SU(4)-based ISA is  $b_{\text{SU}(4)}(n) = \lceil (4^n - 3n - 1)/9 \rceil$ , implying a theoretical 55.6% reduction in #2Q gates compared to a CNOT-based ISA, whose bound is  $b_{\text{CNOT}}(n) = \lceil (4^n - 3n - 1)/4 \rceil$ . While no constructive algorithms can achieve this bound, the *approximate synthesis* technique has demonstrated this capability [34, 43]. Through structural optimization of gate arrangements and numerical optimization of gate parameters, approximate synthesis can generate circuits with fewer gates that are equivalent to a target unitary within a permissible precision [18]. This precision is typically set to be negligible ( $10^{-15}$ - $10^{-10}$ , measured by infidelity  $1 - \frac{1}{N}|\text{Tr}(U^\dagger V)|$ ) compared to physical errors, making the synthesis effectively exact for practical purposes.

**5.1.2 Hierarchical synthesis.** To leverage the theoretical synthesis potential of SU(4) and apply approximate synthesis to large-scale real-world programs, we employ a two-tier hierarchical synthesis approach. It first partitions the original circuit into 2Q blocks, each of which is fused into

an  $SU(4)$  gate. Then, it partitions the circuit, now consisting solely of  $SU(4)$  gates, into  $w$ -qubit blocks to determine if each block can be synthesized with fewer  $SU(4)$  gates through approximate synthesis. Specifically, our compiler conditionally performs approximate synthesis blocks whose  $SU(4)$  number is greater than a threshold  $m_{th}$ . Thus, two hyperparameters need to be carefully considered to strike a trade-off between computational overhead and 2Q gate count reduction effect via approximate synthesis: partitioning granularity  $w$  and 2Q gate count threshold  $m_{th}$ . We determine optimal default values through empirical analysis: **(1) Partition granularity ( $w = 3$ ):** Approximate synthesis is computationally expensive, scaling exponentially with circuit width. We found that 3Q partitioning offers a sweet spot, as 3Q subcircuits frequently contain more gates than the theoretical minimum ( $b_{SU(4)}(3) = 6$ ), providing ample optimization opportunities. In contrast, 4Q partitioning results in too slow computation of underlying approximate synthesis, and its potential for reduction is less frequently realized in practice, as  $b_{SU(4)}(4) = 27$  is too large. **(2) Synthesis threshold ( $m_{th} = 4$ ):** In principle,  $m_{th}$  can be set to the #2Q lower bound, i.e., 6. However, empirical observations indicate that as few as 5 or even 4 gates are often sufficient to approximate 3Q blocks within the permissible precision, suggesting that a more aggressive  $m_{th}$  can yield greater gate count reductions. As shown in Figure 5, this method reduces the #2Q for the `alu-v2_33` circuit from 17 to 11.

**5.1.3 Compactness and DAG compacting.** To assess the circuit partitioning effects, we introduce the metric of *compactness* to guide co-optimization of circuit partitioning and subsequent approximate synthesis: an ideal partition creates highly “unbalanced” blocks, concentrating many gates into a few blocks ripe for synthesis while leaving others sparse. Specifically, we desire that in the second-stage partitioned result,  $w$ -qubit blocks with  $\#2Q > m_{th}$  concentrate more 2Q gates, while those with  $\#2Q \leq m_{th}$  include fewer.

Under the guidance of the compactness metric and the gate scheduling idea, we invent the *DAG compacting* pass to conduct aggressive optimization for partitioned  $SU(4)$ -based subcircuits that comprise a nested DAG. The DAG compacting pass exploits opportunities of exchanging “commutative”  $SU(4)$ s to enhance compactness. For example, a gate sequence like  $[SU(4)_{1,2}, SU(4)_{2,3}]$  can often be exchanged into  $[SU(4)_{2,3}, SU(4)_{1,2}']$  with negligible error (Figure 6). By performing this commutation,  $SU(4)_{1,2}'$  can merge with the subsequent 3Q block  $SU(8)_{0,1,2}$ , thereby increasing compactness. The pass iteratively applies these feasible exchanges to maximize the compactness-increasing opportunities, enabling more aggressive optimization.

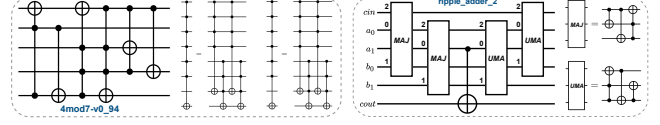


Figure 7. Examples of high-level program IRs.

## 5.2 Global optimization: Program-aware synthesis

The hierarchical synthesis works at the circuit level and will induce diverse parameterized quantum gates thus with uncontrollable calibration overhead. It is impractical for large-scale program compilation on its own. Thus, an approach to globally optimize quantum programs and managing the calibration overhead is necessary.

**5.2.1 Real-world program patterns.** In general, real-world quantum algorithms can be categorized into two types: (1) those solving classical problems, that is, quantum versions of digital logic functions, constructed through binary to qubit encoding, and (2) those solving more quantum or optimization problems, typically constructed through Hamiltonian simulation. For the latter type of programs, there are already highly-effective global compilation techniques that can be seamlessly applied to the  $SU(4)$  ISA, especially for those ISA-independent dedicated compilers such as Rustiq [19], QuCLEAR [41], and Phoenix [68]. Therefore, we focus more on how to globally optimize the first type of quantum programs.

Specifically, these programs are composed of CX/CCX/MCX gates (sometimes with 1Q rotations and Paulis), as exemplified in Figure 7. This feature is ideal for a *template-based synthesis* strategy—first find the optimal synthesis schemes for these high-level semantics and then unroll them within circuits. We refine 3Q blocks as the IRs and constructs their optimal synthesis templates again via approximate synthesis, since intricate components such as Peres [60] and MAJ/UMA [17] are usually represented as 3Q circuits. Moreover, 3Q represents the perfect granularity for efficient yet powerful synthesis as discussed in Section 5.1.2. For MCX, it can be first recursively decomposed into CCX gates [5]. This approach simultaneously enables effective optimization and benefits calibration efficiency by reusing a finite set of highly optimized building blocks.

**5.2.2 Template-based synthesis.** The ReQISC compiler employs a “pre-synthesis followed by assembly” strategy for compiling programs in their high-level IRs. In the *pre-synthesis* stage, all of the circuits are transformed into CCX-based circuits via MCX decomposition [5]. The compiler extracts all distinct 3Q IRs from the benchmark suite, ignoring specific qubit indices, and determines their minimal-#2Q  $SU(4)$  synthesis templates through multiple rounds of approximate synthesis. In the *assembly* stage, the compiler

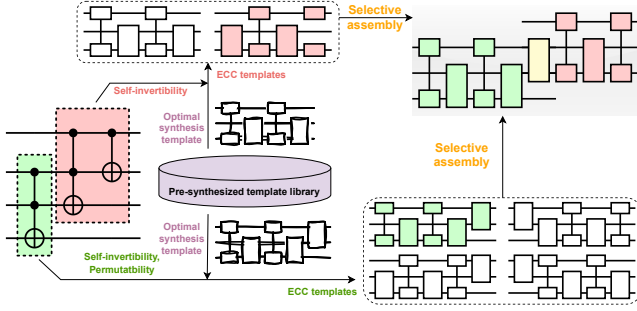


**Figure 8.** Template-based synthesis building on a pre-synthesized template library and the selective assembly strategy.

unrolls 3Q IRs in an input CCX-based circuit into their optimal synthesis schemes building on the pre-synthesized template library. The *equivalent circuit classes (ECC)* of each IR and its  $SU(4)$  synthesis templates are derived, according to the *self-invertibility* and *control-bit permutability* of the 3Q IR. That enables further  $SU(4)$  gate count reduction when selectively assembling near-neighbor IRs from their alternative ECC templates, as two  $SU(4)$ s acting on the same pair of qubits can be fused into one  $SU(4)$ . Figure 8 illustrates this synthesis procedure of a circuit snippet with consecutive Toffoli and Peres gates. Since the distinct 3Q IRs in real-world programs are finite, this template-based approach is computationally efficient and calibration-friendly.

### 5.3 Pushing toward practicality on hardware

**5.3.1 Calibration overhead.** Herein we discuss how the ReSIC compiler overcomes the calibration issue. First, the number of distinct  $SU(4)$ s introduced by template-based synthesis is negligible, as the distinct 3Q IR patterns are finite in real-world applications [63]. It is the hierarchical synthesis pass that incurs appreciable calibration overhead through exhaustive local optimization, in which approximate synthesis inevitably induces more diverse  $SU(4)$ s’ parameters. Therefore, employing the hierarchical synthesis pass means sacrificing calibration efficiency for greater #2Q reduction.

Moreover, naively applying our scheme to variational quantum programs (e.g., QAOA [23], UCCSD [6]) which necessitate multiple runs with variational gate parameters is unrealistic as it requires continual calibration of variational  $SU(4)$ s in experiments. Instead, the workload of reconfiguring variational  $SU(4)$  gates can be shifted to reconfiguring 1Q gates, by decomposing  $SU(4)$ s into a gate set with fixed 2Q gates (e.g., SQISW, B) and parametrized 1Q gates. These 1Q parameters can be easily calibrated with constant experimental overhead by means of the PMW protocol [13, 14, 26, 62], which allows for the implementation of any continuous 1Q gate without explicit calibration by simply tuning the phase shift of microwave pulses. While this compromise may result in a slightly higher 2Q gate count, it represents a necessary trade-off for executing variational algorithms.

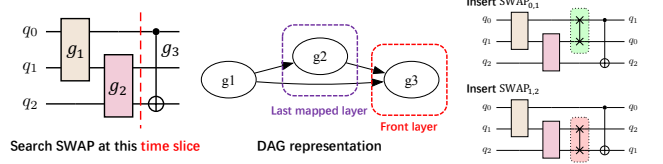


**Figure 9.** The flexibility of SWAP insertions is exploited to mitigate #2Q overhead for qubit mapping on a 1D chain topology ( $q_0 \leftrightarrow q_1 \leftrightarrow q_2$ ). Inserting  $SWAP_{1,2}$  is preferred over  $SWAP_{0,1}$ , as it does not increase # $SU(4)$ .

**5.3.2 Qubit routing.** Even with sophisticated mapping algorithms, significant #2Q overhead is induced during qubit routing by the insertion of SWAP gates [39, 42, 70]. Leveraging the expressiveness of  $SU(4)$ , we develop a dedicated mapping algorithm, *mirroring-SABRE*, by incorporating the  $SU(4)$ -aware SWAP search strategy into the SABRE [39].

Mirroring-SABRE inherits the basic thought of SABRE [39]. SABRE attempts to map 2Q gates layer by layer via extracting the “front layer”  $F$ , peeling executable gates and searching SWAP gates to minimize the heuristic cost  $H$  of the unresolved front layer.  $H$  involving the current front layer and a SWAP candidate is designed to minimize the topological distance between upcoming qubits and promote parallelism. In our proposed mirroring-SABRE, we additionally define the “last mapped layer”  $L$  as the set of 2Q gates that has no succeeding ones within the DAG constructed by already mapped 2Q gates, such that the SWAP search process prioritizes SWAP gates that  $L$  can absorb, as illustrated in Figure 9. We also define an initial heuristic cost function  $H_0(F, DAG, \pi, D)$  before each SWAP search epoch with the similar calculation method relative to the original cost function  $H(F, DAG, \pi, D, SWAP)$  from SABRE. If there is a SWAP candidate that can be absorbed by  $L$  and also leads to a lower  $H$  than  $H_0$ , it will be selected as a SWAP mirroring effect that induces no #2Q overhead. Otherwise, the SWAP search proceeds similarly to SABRE.

Besides the flexibility to modify the SWAP search process, we choose SABRE as the backbone due to its “lookahead” mechanism. As SABRE evaluates qubit distances in upcoming layers apart from the front layer  $F$ , physical qubits involved in the last mapped layer and those within  $F$  tend to aggregate after multiple search periods. This emergent aggregation creates more opportunities to fuse a required SWAP with a preceding 2Q gate, thus reducing routing overhead.

### 5.4 Overall framework and implementation

**5.4.1 End-to-end compilation workflow.** The ReQISC compiler pipeline consists of program-aware template-based synthesis, hardware-agnostic hierarchical synthesis, and finally hardware-aware Mirroring-SABRE routing. We perform the hardware-agnostic optimization before routing to



maximize gate count reduction free from topological constraints. This approach allows us to approach theoretical  $\#SU(4)$  lower bound or less for each subcircuit. We observe that reversing this order provides no benefit while hindering flexibility and scalability.

**5.4.2 Implementation.** The ReQISC compiler is developed in Python to be a self-contained quantum programming SDK. It also operationalizes the ReQISC microarchitecture, enabling the generation of executable  $SU(4)$ -based circuits with control parameters applicable to specific hardware. In case of no available hardware, the output circuits are expressed in  $\{\text{Can}(x, y, z), U3(\theta, \phi, \lambda)\}$ . The approximate synthesis functionality leverages modules of BQSKit [69]. A key feature is its configurable approach to the calibration-performance trade-off. We provide two practical compilation schemes: “ReQISC-Full”, which employs all optimization passes including the hierarchical synthesis for aggressive gate count reduction, and “ReQISC-Red”, which bypasses this pass for minimal calibration overhead.

## 6 Evaluation

We evaluate ReQISC against SOTA counterparts on a comprehensive benchmark suite, demonstrating its superiority spanning multiple hardware types and showing clear advantages in its microarchitecture, as well as in end-to-end logical-level (topology-agnostic) and topology-aware compilation. All experiments ran on an Apple M3 Max laptop.

### 6.1 Experimental setup

**6.1.1 Metrics.** We focus on  $\#2Q$  (2Q gate count), Depth2Q (depth of the circuit involving only 2Q gates), pulse duration, and program fidelity as metrics. The whole circuit duration corresponds to the critical path with the longest pulse duration. Program fidelity is measured by the Hellinger fidelity between noisy simulation and ideal simulation.

**6.1.2 Baselines.** “Qiskit”, “TKet”, and “BQSKit” are three primary baselines for comparison. In Qiskit, the standard O3 transpile pass is used. In Tket, the standard compilation procedure is constructed by sequentially employing PauliSimp and FullPeepholeOptimise passes, in which PauliSimp is the built-in Hamiltonian simulation program optimization engine [15]. To demonstrate that ReQISC’s benefits stem from its co-designed compilation strategy, we also compare against three variants: “Qiskit- $SU(4)$ ” and “TKet- $SU(4)$ ”, with a pass that partitions and fuses 2Q gates into  $SU(4)$ s appended to the standard Qiskit/TKet compilation procedure, and “BQSKit- $SU(4)$ ”, which employs its compile pass by designating a customized  $\{\text{Can}, U3\}$  gate set.

**6.1.3 Benchmarks.** The benchmark suite comprises 132 programs from 17 diverse categories (alu, encoding, uccsd,

etc.). Program sizes as indicated by  $\#2Q$  in CNOT-based circuit representation range from several to  $10^4$ . Most programs are selected from published benchmark suites [57, 63].

Notations of most benchmarks align with those used in published benchmark suites for which we refer readers to RevLib’s website and TKet’s benchmarking repo. For benchmarks whose high-level algorithmic description is in form of a .real file involving MCX gates, we convert them into CCX-based circuits as the input for the ReQISC compiler and further decompose them into CNOT-based circuits as the input for the baselines. For variational quantum programs, Pauli strings with coefficients are compiled into  $SU(4)$  gate sequences by the high-level ISA-independent Phoenix compiler [68] before being used as input for the ReQISC compiler, while CNOT-based circuits are fed to baselines.

**6.1.4 Hardware assumptions.** The ReQISC microarchitecture is evaluated under representative coupling Hamiltonians, including XY, XX, and random couplings. Since XY coupling aligns with the mainstream flux-tunable superconducting platforms (e.g., Google’s Sycamore [3]), it is the default assumption for pulse-level benchmarking and fidelity experiments. Baselines are compared using their conventional, optimized pulse implementations for CNOT, iSWAP, and SQiSW gates under XY coupling [3, 29, 37].

### 6.2 Performance of ReQISC microarchitecture

We quantitatively benchmark the ReQISC microarchitecture by computing the average pulse duration to synthesize  $10^5$  Haar-random  $SU(4)$  unitaries (Table 2). For mainstream XY-coupled platforms, ReQISC slashes the average synthesis cost to just  $1.341 g^{-1}$ —a nearly five-fold improvement over the  $6.664 g^{-1}$  ( $3 \times \pi/\sqrt{2} \approx 6.664$  [37]) required by conventional CNOT gate scheme. This superior efficiency is not limited to a specific hardware interaction; ReQISC also achieves an average duration of  $1.178 g^{-1}$  for XX coupling and  $1.321 g^{-1}$  for arbitrary random couplings. These results demonstrate that a full  $SU(4)$  ISA, when powered by our microarchitecture, is fundamentally more performant than conventional approaches. Furthermore, our scheme is so efficient that even when used to realize a fixed gate like SQiSW, its performance is nearly on par (within a 1.6x factor) with that of the fully arbitrary  $SU(4)$  implementation.

### 6.3 Logical-level compilation

As detailed in Table 1, ReQISC delivers substantial improvements over all baselines across every key metric. Particularly, ReQISC consistently slashes the total pulse-level circuit duration by 40%–90% across all benchmarks, with an overall average of 68% (73%) for ReQISC-Red (ReQISC-Full). We note that the difference between the results for ReQISC-Red versus ReQISC-Full is much more pronounced for non-variational quantum programs, suggesting that they benefit more from local optimization via hierarchical synthesis. That aligns with

**Table 1.** Logical-level compilation comparisons in terms of the reduction rates of #2Q, Depth2Q, and pulse duration  $T$ . Metrics within the merged column “Benchmarks info.” indicate the circuit-level and pulse-level metrics for quantum programs in its original CNOT-based representation.  $T$  is in unit  $g^{-1}$ . Red./Full. indicates ReQISC-Red/Full compiler. For near-identity  $SU(4)$  gates (occurring in qft, pf, qaoa and uccsd), the gate mirroring technique introduced in Section 3 is employed. Throughout we assume the XY-coupled Hamiltonian where the baseline CNOT scheme has gate duration  $\tau = \pi/\sqrt{2}g$ .

Benchmarks info.					Avg. reduction of #2Q (%)					Avg. reduction of Depth2Q (%)					Avg. reduction of Duration (%)				
Category (#)	#Qubit	#2Q	Depth2Q	Duration $T$	Qiskit	TKet	BQSKit	Red.	Full.	Qiskit	TKet	BQSKit	Red.	Full.	Qiskit	TKet	BQSKit	Red.	Full.
alu (12)	5-6	15-192	12-166	26.7-368.8	1.54	1.72	8.12	29.83	32.01	1.85	2.20	9.20	26.41	28.40	1.85	2.20	9.20	52.41	54.48
bit_adder (13)	4-15	14-5.1k	13-3.8k	28.9-8.5k	9.43	9.70	13.81	33.01	40.38	8.21	8.36	11.33	22.75	30.45	8.21	8.36	11.33	52.57	56.14
comp (19)	5-6	13-155	12-134	26.7-297.7	1.13	6.66	6.15	27.56	32.50	1.29	7.11	3.86	21.91	26.25	1.29	7.11	3.86	47.17	50.44
encoding (9)	3-15	10-3.3k	10-2.5k	22.2-5.6k	5.66	7.78	13.20	36.49	38.88	5.66	7.86	12.40	33.94	36.46	5.66	7.86	12.40	57.15	59.14
grover (1)	9-9	288-288	228-228	506.5-506.5	0.00	0.00	17.36	44.44	44.44	0.00	0.00	20.61	30.70	30.70	0.00	0.00	20.61	53.69	53.69
hwb (12)	4-170	26-4.4k	25-3.5k	55.5-7.8k	1.28	3.62	9.95	25.89	31.80	1.20	4.09	10.69	27.18	34.17	1.20	4.09	10.69	51.52	58.11
modulo (8)	5-7	9-62	8-56	17.8-124.4	9.64	9.84	14.92	34.18	38.90	10.67	10.67	15.51	32.49	38.80	10.67	10.67	15.51	58.94	62.74
mult (3)	12-48	99-1.6k	60-293	133.3-650.9	0.00	0.25	0.00	16.05	16.05	0.00	0.24	0.00	11.53	11.53	0.00	0.24	0.00	41.00	41.00
pf (9)	10-30	60-1.8k	60-1.8k	133.3-4.0k	0.96	27.41	2.20	87.59	87.59	0.96	71.85	3.46	98.63	98.63	0.96	71.85	3.46	98.70	98.70
qaoa (9)	8-24	192-13.2k	60-1.2k	133.3-2.7k	0.00	0.00	0.00	58.47	58.47	0.00	0.00	0.00	70.96	70.96	0.00	0.00	0.00	80.78	80.78
qft (3)	8-32	56-612	26-122	57.8-271.0	0.00	0.00	0.00	50.00	50.00	0.00	0.00	0.00	50.00	50.00	0.00	0.00	0.00	50.77	50.77
rip_add (4)	12-62	81-481	68-393	151.1-873.0	0.00	6.21	12.37	31.06	49.57	0.00	0.72	11.86	30.82	39.07	0.00	0.72	11.86	53.75	58.69
square (3)	10-13	745-3.8k	547-3.0k	1.2k-6.6k	0.02	0.20	9.49	31.42	38.16	0.00	0.26	5.59	19.75	24.25	0.00	0.26	5.59	45.98	50.95
sym (6)	7-14	107-29.3k	63-22.1k	140.0-49.1k	3.42	3.86	9.67	30.16	35.42	0.62	1.31	4.67	18.93	23.81	0.62	1.31	4.67	45.92	50.75
tof (4)	5-19	18-102	15-78	33.3-173.3	0.00	4.46	0.00	30.29	30.29	0.00	3.51	0.00	12.38	12.38	0.00	3.51	0.00	39.39	39.39
uccsd (14)	8-14	630-14.4k	615-13.6k	1.4k-30.2k	23.46	64.03	6.71	76.50	84.11	23.49	67.53	7.48	78.45	85.63	23.49	67.53	7.48	84.02	89.25
urf (3)	8-9	9.0k-23.6k	7.3k-18.6k	16.2k-41.3k	0.91	4.47	6.81	20.61	25.90	0.83	4.66	3.30	14.34	20.77	0.83	4.66	3.30	42.71	48.55
Overall (132)					5.34	15.91	7.99	46.95	51.89	5.2	21.83	7.34	53.43	57.5	5.2	21.83	7.34	68.03	71.0

**Table 2.** Synthesis cost comparison in terms of gate duration  $\tau$  ( $g^{-1}$ ) achieved by the ReQISC microarchitecture. The Haar-random average cost (number of basis gates for synthesizing arbitrary  $SU(4)$  gates) for CNOT, iSWAP, SQISW, B gates are 3, 3, 2.21, and 2, respectively.

Coupling type	XY coupling		XX coupling		Random	
Basis gate	$\tau$ (Sgl.)	$\tau$ (Avg.)	$\tau$ (Sgl.)	$\tau$ (Avg.)	$\tau$ (Sgl.)	$\tau$ (Avg.)
CNOT	2.221	6.664	—	—	—	—
$SU(4)$	—	1.341	—	1.178	—	1.321
CNOT	1.571	4.712	0.785	2.356	1.228	3.684
iSWAP	1.571	4.712	1.571	4.712	1.898	5.693
SQISW	0.785	1.736	0.785	1.736	0.949	2.097
B	1.571	4.712	1.178	2.356	1.435	2.869

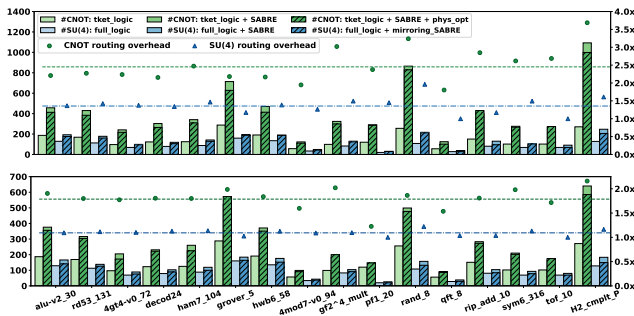


**Figure 10.** topology-aware benchmarking for 1D-chain (upper) and 2D-grid (bottom) mapping.  $\_logic$ : compilation on logical circuits without mapping;  $phys\_opt$ : optimization on physical circuits by means of Qiskit’s topology-preserving O3 transpile. Green dots and blue triangles indicate the multiples of #2Q after optimized qubit mapping (hatched-green or hatched-blue) relative to logical circuits (light-green or light-blue). Dashed horizontal lines refer to the geometric-mean overheads.

our expectation since these arithmetic-logic-like programs exhibit versatile subcircuit patterns.

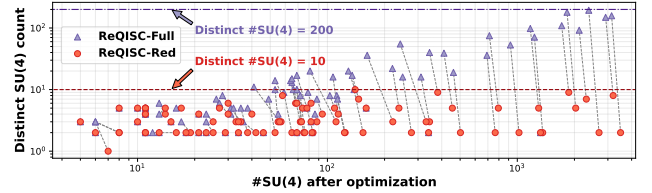


**Figure 11.** Trade-off between calibration overhead and #2Q reduction (ReQISC-Red v.s. ReQISC-Full). Each connected pair of points corresponds to a quantum program instance. Scaling trends remain consistent for larger circuits (not shown due to fewer data points).

Qiskit-SU(4)	15.66	20.78	19.54	20.16	16.67	16.43	19.93	16.05	50.40	50.00	50.00	12.43	16.65	18.61	16.67	34.80	14.51
TKet-SU(4)	15.80	20.94	20.91	20.82	16.67	18.10	20.14	16.30	52.74	50.00	50.00	18.64	16.71	18.94	18.09	65.20	17.02
BQSKit-SU(4)	29.22	28.96	24.88	32.66	34.03	25.32	30.11	16.03	50.67	50.00	49.75	35.00	26.23	26.44	16.67	71.96	21.42
ReQISC-NC	30.77	35.10	31.19	38.03	44.44	28.08	35.31	16.05	87.59	58.47	50.00	37.28	36.99	32.91	30.29	82.28	23.00
ReQISC-Full	32.01	40.38	32.50	38.88	44.44	31.80	38.90	16.05	87.59	58.47	50.00	49.57	38.16	35.42	30.29	84.11	25.90

**Figure 12.** Ablation study benchmarking results.

#### 6.4 Topology-aware compilation

Figure 10 illustrates ReQISC’s performance with qubit mapping/routing, across a set of medium-scale benchmarks from each category. Results show that mirroring-SABRE outperforms conventional SABRE paired with ReQISC, with #2Q reduction up to 28.2% (23.7%) and on average 11.0% (15.7%) for 1D-chain (2D-grid) qubit mapping. This effect is also program-dependent—for instance, mirroring-SABRE incurs no additional #2Q overhead on qft\_8 and tof\_10. The advantage is even more pronounced when comparing the end-to-end ReQISC compilation against the SOTA CNOT-based

baseline (hatched-blue v.s. hatched-green in Figure 10). Specifically, the geometric mean of  $\#SU(4)$  overhead is 1.36x (1.09x) for 1D-chain (2D-grid) mapping; for  $\#CNOT$ , it is 2.45x (1.79x). These results highlight the fundamental superiority of ReQISC for compiling to realistic hardware.

### 6.5 Calibration efficiency v.s. $\#2Q$ reduction

We evaluate the trade-off between calibration overhead and  $2Q$  gate count reduction by comparing the number of distinct  $SU(4)$  gates in circuits compiled by ReQISC-Red and ReQISC-Full for benchmarks with  $\#2Q$  up to 5000. As shown in Figure 11, ReQISC-Red has negligible calibration overhead as expected, with distinct  $SU(4)$ s below 10. In field tests, only 56 distinct  $3Q$  subcircuit structures were found across all benchmarks except variational programs. For ReQISC-Full, calibration overhead is reasonable, typically below 200. This demonstrates a practical and controllable trade-off for users seeking the highest performance, allowing them to balance gate fidelity with experimental complexity.

### 6.6 Ablation study and Breakdown analysis

**6.6.1 Efficacy of specialized passes.** To isolate the benefits of our co-designed compilation strategy, we perform ablation study for ReQISC-Full against Qiskit- $SU(4)$ , TKet- $SU(4)$ , and BQSKit- $SU(4)$ . As shown in Figure 12, ReQISC-Full still significantly outperforms these variants, confirming that its global program-aware and hierarchical synthesis passes are critical for effective  $SU(4)$  compilation. Notably, while BQSKit- $SU(4)$  achieves a reasonable gate count reduction, it is impractical due to an explosion of distinct  $SU(4)$  gates, which implies an uncontrollable calibration overhead. In contrast, ReQISC-Full maintains a manageable, sub-linearly scaling set of distinct gates—an order of magnitude fewer in our tests (Figure 11).

**6.6.2 Impact of DAG Compacting.** Our breakdown analysis confirms the importance of the DAG compacting pass. We first observed that different circuit partitioning strategies had a negligible impact on performance (less than 2% variation). The DAG compacting pass, however, is crucial. Comparing ReQISC-Full against a version without this pass (“ReQISC-NC”) reveals substantial gains. As shown in Figure 12, this single pass improves the  $\#2Q$  reduction rate by up to 33% (e.g., for `rip_add` benchmarks), demonstrating its effectiveness in exploiting approximate commutation rules.

### 6.7 Fidelity experiment

We performed noisy simulations by QSim [59] on twelve representative benchmarks, comparing ReQISC against a SOTA CNOT-based workflow (TKet with SABRE mapping). Our model assumed a XY-coupled device with the depolarizing channel appended to  $2Q$  gates, where error rates were scaled proportionally to the gate duration ( $\tau$ ) of each CNOT ( $\tau_0 = \pi/\sqrt{2}g^{-1}$ ;  $p_0 = 0.001$ ) or  $SU(4)$  operation

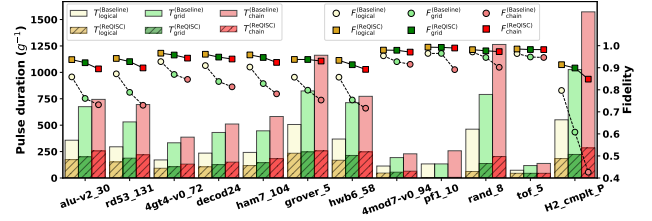


Figure 13. Program fidelity  $F$  and pulse duration  $T$  comparison.

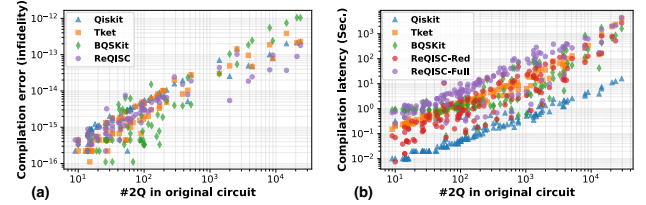


Figure 14. Compilation errors (a) and latency (b) comparison.

( $\tau$ ;  $p = p_0\tau/\tau_0$ ). As shown in Figure 13, ReQISC delivers substantially higher fidelity and faster execution across the board. At the logical level (all-to-all topology), it achieves an average 2.36x error reduction and a 3.06x execution speedup. These advantages become even more pronounced when mapping to topology-constrained devices, with error reductions of 3.18x (2D grid) and 3.34x (1D chain), and corresponding speedups of 4.30x and 4.55x, respectively.

### 6.8 Reliability and scalability

For benchmarks with up to eleven qubits, we verify the compiled circuits generated by baselines and the ReQISC compiler, by computing the compilation error quantified by circuit infidelity. Figure 14 (a) shows all compilers exhibit a similar level of compilation errors. This is expected, as the approximate synthesis is de facto “numerically exact” for every subcircuit synthesis, whose correctness is bounded by the IEEE754 machine precision  $\approx 2.2 \times 10^{-16}$ . The extensive peephole optimizations (e.g., block consolidation, KAK decomposition) within Qiskit/TKet can only be at the level of machine precision as well. Note that both  $x$  and  $y$  axes use logarithmic scaling—for large circuits, ReQISC/Qiskit/TKet’s compilation errors are bounded much better than BQSKit.

The ReQISC compiler’s computational complexity is polynomial in program size, as its key passes have linear or polynomial complexity. Figure 14 (b) confirms that both ReQISC-Red and ReQISC-Full scale well in their runtime, despite being implemented in Python. ReQISC-Red is consistently more efficient than TKet (C++ backend) and BQSKit (Rust backend). ReQISC-Full, which performs heavy optimizations, offers performance competitive with BQSKit, demonstrating that its substantial gate count reduction is achieved with a practical and acceptable increase in compilation time.

## 7 Conclusion

CNOT-based ISAs are the predominant choice for most hardware platforms. Although some continuous gate families have been proposed and experimentally demonstrated, they are generally impractical due to suboptimal or non-native implementation, excessive calibration overhead, and limited compilation strategies. The presented ReQISC uses the most expressive SU(4) ISA that is optimally realized by means of our microarchitecture. Our approach for the first time enables the straightforward implementation of any equivalent 2Q gate under arbitrary coupling Hamiltonians, with simple pulse control and minimal gate time. Supported by the end-to-end ReQISC compiler, we can strike an excellent balance between performance and calibration overhead, thereby challenging traditional notions of the two being fundamentally in contradiction.

The implications of this work are significant for quantum computing both in the near and long term. For the fault-tolerant regime [2, 54], our approach offers multifaceted advantages: it provides a pathway to faster and higher-fidelity logical qubits (e.g., via a  $\sqrt{2}x$  faster CNOT on XY-coupled hardware) and enables native support for Clifford operations like iSWAP and SWAP that proves critical for state-of-the-art QEC schemes [22, 44, 65, 74]. By providing the architecture and compiler to leverage a richer, more expressive native gate set, ReQISC opens new avenues for designing performant and scalable quantum computers.

## References

- [1] Deanna M Abrams, Nicolas Didier, Blake R Johnson, Marcus P da Silva, and Colm A Ryan. 2020. Implementation of XY entangling gates with a single calibrated pulse. *Nature Electronics* 3, 12 (2020), 744–750.
- [2] Rajeev Acharya, Dmitry A. Abanin, Laleh Aghababaie-Beni, Igor Aleiner, Trond I. Andersen, Markus Ansmann, Frank Arute, Kunal Arya, Abraham Asfaw, Nikita Astrakhantsev, Juan Atalaya, Ryan Babbush, Dave Bacon, Brian Ballard, Joseph C. Bardin, Johannes Bausch, Andreas Bengtsson, Alexander Bilmes, Sam Blackwell, Sergio Boixo, Gina Bortoli, Alexander Boussass, Jenna Bovaird, Leon Brill, Michael Broughton, David A. Browne, Brett Buchea, Bob B. Buckley, David A. Buell, Tim Burger, Brian Burkett, Nicholas Bushnell, Anthony Cabrera, Juan Campero, Hung-Sheng Chang, Yu Chen, Zijun Chen, Ben Chiaro, Desmond Chik, Charina Chou, Jalan Claes, Amenta Y. Clambaneanu, Josh Cong, Roberto Collins, Paul Conner, William Cournier, Alexander L. Crook, Ben Curtin, Sayan Das, Alex Davies, Laura De Lorezzo, Dristo M. Debry, Sean Denver, Michael Devoret, Augustin Di Paolo, Paul Donoho, Illy Drozdov, Andrew Dunsworth, Clint Eark, Thanes Elich, Alec Eickbusch, Aviv Moshe Elbag, Mahmoud Elzouka, Catherine Erickson, Lara Faoro, Edward Farhi, Vincicus S. Ferreira, Leslie Fores Burgos, Ebrahim Forati, Austin G. Fowler, Brooks Foxen, Subas Ganjam, Gonzalo Garcia, Robert Gasca, Elie Genois, William Giang, Craig Gidney, Dar Gilboa, Rajan Gokhale, Alejandro Grajales Daul, Dietrich Grauman, Alex Greene, Jonathan A. Gross, Steve Habegger, John Hall, Michael C. Hamilton, Monica Hansen, Matthew Harrigan, Sean D. Harrington, Francisco J.H. Heras, Stephen Hincks, Paula Hoel, Oscar Higgott, Gordon Hill, Jeremy Hilton, George Holland, Sabrina Hong, Hsin-Yuan Huang, Ashley Huff, William J. Huggins, Lev B. Ioffe, Sergei V. Isakov, J. Justin Iveland, Evan Jeffrey, Zhang Jiang, Cody Jones, Stephen Jordan, Chitail John, Pavol Juhas, Dvir Kafri, Hui Kang, Amir H. Karamlou, Kostantyn Kechedzhi, Julian Kelly, Trupti Khair, Tanuj H. Khattar, Seon Kim, Paul V. Klimov, Andrey R. Klots, Bryce Kobrin, Pushmeet Kohli, Alexander N. Korotkov, Fedor Kostritsa, Robin Kothari, Borislav Kozlovskii, John Mark Kreikebaum, Vladislav D. Kurilovich, Nathan Lacroix, David Landhuis, Tiano Lange-Dei, Brandon W. Langley, Pavel Laptev, Kim-Ming Lau, Loick Le Guevel, Justin Ledford, Joonho Lee, Kennley Lee, Yuri D. Lensky, Shannon Leon, Brian J. Lester, Wing Yan Li, Yin Li, Alexander T. Lili, Wayee Liu, William P. Livingston, Aditya Locharla, Erik Lucero, Daniel Lundahl, Aaron Luni, Sid Madhuk, Finnon D. Malone, Ashley Maloney, Salvatore Mandra, James Manyika, Leigh S. Martin, Orion Martin, Steven Martin, Cameron Marfield, Jarrod R. McClean, Matt McEwen, Seneca Meeks, Anthony Megrant, Xiao Mi, Kevin C. Miao, Amanda Mieszala, Reza Mola, Sebastian Molina, Shirin Montazeri, Alexis Morvan, Ramis Moussa, Wojciech Muczkiewicz, Ofer Naaman, Matthew Neeley, Charles Neil, Ani Nersisyan, Hartmut Neven, Michael Newman, Jun How Ng, Anthony Nguyen, Murray Nguyen, Chia-Hung Ni, Murphy Yuezhen Niu, Thomas E. O'Brien, William D. Oliver, Alex Opremcak, Kristoffer Ottosson, Andre Petukhov, Alex Pizzito, John Platt, Rebecca Potter, Orion Pritchard, Leonid P. Pryadko, Chris Quintana, Ganesh Ramachandran, Matthew J. Reagor, John Redding, Dadi M. Rados, Gabrielle Roberts, Elliott Rosenberg, Emma Rosenfeld, Pedram Roushan, Nicholas C. Rubin, New Year Saei, Daniel Sank, Kannan Sankaragomathi, Kevin J. Satzinger, Henry F. Schurkus, Christopher Schuster, Andrew W. Senior, Michael J. Shearn, Aaron Shorter, Noah Shutter, Vladimir Shvarts, Shradha Singh, Volodymyr Sivak, Jindra Skrzny, Spencer Small, Vadim Smelyanskiy, W. Clarke Smith, Rolando Somma, Sofia Springer, George Sterling, Doug Strain, Jordan Suchard, Aaron Szasz, Alex Szein, Douglas Thor, Alfredo Torres, M. Mert Torubaldi, Abeer Vishnav, Justin Vargas, Sergey Vdovichev, Guifre Vidal, Benjamin Villalonga, Catherine Vollgraff Heidweiller, Steven Waltman, Shannon X. Wang, Brayden Ware, Kate Weber, Travis Weidel, Theodore White, Kristi Wong, Bryan W.K. Woo, Cheng Xing, Z. Jamie Yao, Ping Yeh, Bicheng Ying, Juhwan Yoo, Nourelin Yost, Grayson Young, Adam Zalcman, Yaxing Zhang, Ningfeng Zhu, and Nicholas Zobrist. 2024. Quantum error correction below the surface code threshold. *Nature* 638, 8052 (2024), 920.
- [3] Frank Arute, Kunal Arya, Ryan Babbush, Dave Bacon, Joseph C. Bardin, Rami Barends, Rupak Biswas, Sergio Boixo, Fernando G. S. L. Brandao, David A. Buell, Brian Burkett, Yu Chen, Zijun Chen, Ben Chiaro, Roberto Collins, William Courtney, Andrew Dunsworth, Edward Farhi, Brooks Foxen, Austin Fowler, Craig Gidney, Marissa Giustina, Rob Graff, Keith Guerin, Steve Habegger, Matthew P. Harrigan, Michael J. Hartmann, Alan Ho, Markus Hoffmann, Trent Huang, Travis S. Humble, Sergei V. Isakov, Evan Jeffrey, Zhang Jiang, Dvir Kafri, Kostyantyn Kechedzhi, Julian Kelly, Paul V. Klimov, Sergey Knysh, Alexander Korotkov, Fedor Kostritsa, David Landhuis, Mike Lindmark, Erik Lucero, Dmitry Lyakh, Salvatore Mandrà, Jarrod R. McClean, Matthew McEwen, Anthony Megrant, Xiao Mi, Kristel Michielsen, Masoud Mohseni, Josh Mutus, Ofer Naaman, Matthew Neeley, Charles Neill, Murphy Yuezhen Niu, Eric Ostby, Andre Petukhov, John C. Platt, Chris Quintana, Eleanor G. Rieffel, Pedram Roushan, Nicholas C. Rubin, Daniel Sank, Kevin J. Satzinger, Vadim Smelyanskiy, Kevin J. Sung, Matthew D. Trevithick, Amit Vainsencher, Benjamin Villalonga, Theodore White, Z. Jamie Yao, Ping Yeh, Adam Zalcman, Hartmut Neven, and John M. Martinis. 2019. Quantum supremacy using a programmable superconducting processor. *Nature* 574, 7779 (2019), 505–510.
- [4] Feng Bao, Hao Deng, Dawei Ding, Ran Gao, Xun Gao, Cupjin Huang, Xun Jiang, Hsiang-Sheng Ku, Zhisheng Li, Xizheng Ma, et al. 2022. Fluxonium: An alternative qubit platform for high-fidelity operations. *Physical review letters* 129, 1 (2022), 010502.
- [5] Adriano Barenco, Charles H Bennett, Richard Cleve, David P DiVincenzo, Norman Margolus, Peter Shor, Tycho Sleator, John A Smolin,



- and Harald Weinfurter. 1995. Elementary gates for quantum computation. *Physical Review A* 52, 5 (1995), 3457.
- [6] Panagiotis Kl Barkoutsos, Jerome F Gonthier, Igor Sokolov, Nikolaj Moll, Gian Salis, Andreas Fuhrer, Marc Ganzhorn, Daniel J Egger, Matthias Troyer, Antonio Mezzacapo, et al. 2018. Quantum algorithms for electronic structure calculations: Particle-hole Hamiltonian and optimized wave-function expansions. *Physical Review A* 98, 2 (2018), 022322.
- [7] Daniel Barredo, Henning Labuhn, Sylvain Ravets, Thierry Lahaye, Antoine Browaeys, and Charles S Adams. 2015. Coherent excitation transfer in a spin chain of three Rydberg atoms. *Physical review letters* 114, 11 (2015), 113002.
- [8] Charles H Bennett, JI Cirac, Matthew S Leifer, Debbie W Leung, Noah Linden, Sandu Popescu, and Guifre Vidal. 2002. Optimal simulation of two-qubit Hamiltonians using general local operations. *Physical Review A* 66, 1 (2002), 012305.
- [9] Michael J Bremner, Christopher M Dawson, Jennifer L Dodd, Alexei Gilchrist, Aram W Harrow, Duncan Mortimer, Michael A Nielsen, and Tobias J Osborne. 2002. Practical scheme for quantum computation with any two-qubit entangling gate. *Physical Review Letters* 89, 24 (2002), 247902.
- [10] Stephen S Bullock and Igor L Markov. 2003. An arbitrary two-qubit computation in 23 elementary gates or less. In *Proceedings of the 40th Annual Design Automation Conference*. IEEE, Anaheim, CA, USA, 324–329.
- [11] Jianxin Chen, Dawei Ding, Weiyuan Gong, Cupjin Huang, and Qi Ye. 2024. One Gate Scheme to Rule Them All: Introducing a Complex Yet Reduced Instruction Set for Quantum Computing. In *Proceedings of the 29th ACM International Conference on Architectural Support for Programming Languages and Operating Systems, Volume 2*. ACM, La Jolla, CA, USA, 779–796.
- [12] Jianxin Chen, Dawei Ding, and Cupjin Huang. 2022. Randomized benchmarking beyond groups. *PRX Quantum* 3, 3 (2022), 030320.
- [13] Jianxin Chen, Dawei Ding, Cupjin Huang, and Qi Ye. 2023. Compiling arbitrary single-qubit gates via the phase shifts of microwave pulses. *Physical Review Research* 5, 2 (2023), L022031.
- [14] Zhen Chen, Weiyang Liu, Yanjun Ma, Weijie Sun, Ruixia Wang, He Wang, Huikai Xu, Guangming Xue, Haisheng Yan, Zhen Yang, Jiayu Ding, Yang Gao, Feiyu Li, Yujia Zhang, Zikang Zhang, Yirong Jin, Haifeng Yu, Jianxin Chen, and Fei Yan. 2025. Efficient implementation of arbitrary two-qubit gates using unified control. *Nature Physics* (15 Aug 2025). doi:10.1038/s41567-025-02990-x
- [15] Alexander Cowntan, Silas Dilkes, Ross Duncan, Will Simmons, and Seyon Sivarajah. 2019. Phase gadget synthesis for shallow circuits. *arXiv preprint arXiv:1906.01734* (2019).
- [16] Andrew W Cross, Lev S Bishop, Sarah Sheldon, Paul D Nation, and Jay M Gambetta. 2019. Validating quantum computers using randomized model circuits. *Physical Review A* 100, 3 (2019), 032328.
- [17] Steven A. Cuccaro, Thomas G. Draper, Samuel A. Kutin, and David Petrie Moulton. 2004. A new quantum ripple-carry addition circuit. *arXiv preprint quant-ph/0410184*.
- [18] Marc Grau Davis, Ethan Smith, Ana Tudor, Koushik Sen, Irfan Siddiqi, and Costin Iancu. 2019. Heuristics for quantum compiling with a continuous gate set. 12 pages. *arXiv preprint arXiv:1912.02727*.
- [19] Timothée Goubault de Brugière and Simon Martiel. 2024. Faster and shorter synthesis of Hamiltonian simulation circuits. *arXiv:2404.03280 [quant-ph]*
- [20] Jurgen Dijkema, Xiao Xue, Patrick Harvey-Collard, Maximilian Rimbach-Russ, Sander L de Snoo, Guoji Zheng, Amir Sammak, Giorano Scappucci, and Lieven MK Vandersypen. 2025. Cavity-mediated iSWAP oscillations between distant spins. *Nature Physics* 21, 1 (2025), 168–174.
- [21] Wolfgang Dür, Guifre Vidal, Juan Ignacio Cirac, Noah Linden, and Sandu Popescu. 2001. Entanglement capabilities of nonlocal Hamiltonians. *Physical Review Letters* 87, 13 (2001), 137901.
- [22] Alec Eickbusch, Matt McEwen, Volodymyr Sivak, Alexandre Bourassa, Juan Atalaya, Jahan Claes, Dvir Kafri, Craig Gidney, Christopher W. Warren, Jonathan Gross, Alex Opremcak, Nicholas Zobrist, Kevin C. Miao, Gabrielle Roberts, Kevin J. Satzinger, Andreas Bengtsson, Matthew Neeley, William P. Livingston, Alex Greene, Rajeev Acharya, Laleh Aghababae Beni, Georg Aigeldinger, Ross Alcaraz, Trond I. Andersen, Markus Ansmann, Frank Arute, Kunal Arya, Abraham Asfaw, Ryan Babbush, Brian Ballard, Joseph C. Bardin, Alexander Bilmes, Jenna Bova, Dylan Bowers, Leon Brill, Michael Broughton, David A. Browne, Brett Buchea, Bob B. Buckley, Tim Burger, Brian Burkett, Nicholas Bushnell, Anthony Cabrera, Juan Campero, Hung-Shen Chang, Ben Chiaro, Liang-Ying Chih, Agnetta Y. Cleland, Josh Cogan, Roberto Collins, Paul Conner, William Courtney, Alexander L. Crook, Ben Curtin, Sayan Das, Alexander Del Toro Barba, Sean Demura, Laura De Lorenzo, Agustin Di Paolo, Paul Donohoe, Ilya K. Drozdov, Andrew Dunsworth, Aviv Moshe Elbag, Mahmoud Elzouka, Catherine Erickson, Vinicius S. Ferreira, Leslie Flores Burgos, Ebrahim Forati, Austin G. Fowler, Brooks Foxen, Suhas Ganjam, Gonzalo Garcia, Robert Gasca, Élie Genois, William Jiang, Dar Gilboa, Raja Gosula, Alejandro Grajales Dau, Dietrich Graumann, Tan Ha, Steve Habegger, Monica Hansen, Matthew P. Harrigan, Sean D. Harrington, Stephen Heslin, Paula Heu, Oscar Higgott, Reno Hiltermann, Jeremy Hilton, Hsin-Yuan Huang, Ashley Huff, William J. Huggins, Evan Jeffrey, Zhang Jiang, Xiaoxuan Jin, Cody Jones, Chaitali Joshi, Pavol Juhas, Andreas Kabel, Hui Kang, Amir H. Karamlou, Kostyantyn Kechedzhi, Trupti Khair, Tanuj Khattar, Mostafa Khezri, Seon Kim, Bryce Kobrin, Alexander N. Korotkov, Fedor Kostritsa, John Mark Kreikebaum, Vladislav D. Kurilovich, David Landhuis, Tiano Lange-Dei, Brandon W. Langley, Kim-Ming Lau, Justin Ledford, Kenny Lee, Brian J. Lester, Loïc Le Guevel, Wing Yan Li, Alexander T. Lill, Aditya Locharla, Erik Lucero, Daniel Lundahl, Aaron Lunt, Sid Madhuk, Ashley Maloney, Salvatore Mandrà, Leigh S. Martin, Orion Martin, Cameron Maxfield, Jarrod R. McClean, Seneca Meeks, Anthony Megrant, Reza Molavi, Sebastian Molina, Shirin Montazeri, Ramis Movassagh, Michael Newman, Anthony Nguyen, Murray Nguyen, Chia-Hung Ni, Logan Oas, Raymond Orosco, Kristoffer Ottosson, Alex Pizzuto, Rebecca Potter, Orion Pritchard, Chris Quintana, Ganesh Ramachandran, Matthew J. Reagor, David M. Rhodes, Elliott Rosenberg, Elizabeth Rossi, Kannan Sankaragomathi, Henry F. Schurkus, Michael J. Shearn, Aaron Shorter, Noah Shutt, Vladimir Shvarts, Spencer Small, W. Clarke Smith, Sofia Springer, George Sterling, Jordan Suchard, Aaron Szasz, Alex Szein, Douglas Thor, Eifu Tomita, Alfredo Torres, M. Mert Torunbalci, Abeer Vaishnav, Justin Vargas, Sergey Vdovichev, Guifre Vidal, Catherine Vollgraff Heidweiller, Steven Waltman, Jonathan Waltz, Shannon X. Wang, Brayden Ware, Travis Weidel, Theodore White, Kristi Wong, Bryan W. K. Woo, Maddy Woodson, Cheng Xing, Z. Jamie Yao, Ping Yeh, Bicheng Ying, Juhwan Yoo, Noureldin Yosri, Grayson Young, Adam Zalcman, Yaxing Zhang, Ningfeng Zhu, Sergio Boixo, Julian Kelly, Vadim Smelyanskiy, Hartmut Neven, Dave Bacon, Zijun Chen, Paul V. Klimov, Pedram Roushan, Charles Neill, Yu Chen, and Alexis Morvan. 2025. Demonstration of dynamic surface codes. *Nature Physics* (2025), 1–8.
- [23] Edward Farhi, Jeffrey Goldstone, and Sam Gutmann. 2014. A quantum approximate optimization algorithm. *arXiv preprint arXiv:1411.4028* (2014).
- [24] B. Foxen, C. Neill, A. Dunsworth, P. Roushan, B. Chiaro, A. Megrant, J. Kelly, Zijun Chen, K. Satzinger, R. Barends, F. Arute, K. Arya, R. Babbush, D. Bacon, J.C. Bardin, S. Boixo, D. Buell, B. Burkett, Yu Chen, R. Collins, E. Farhi, A. Fowler, C. Gidney, M. Giustina, R. Graff, M. Harrigan, T. Huang, S.V. Isakov, E. Jeffrey, Z. Jiang, D. Kafri, K. Kechedzhi, P. Klimov, A. Korotkov, F. Kostritsa, D. Landhuis, E. Lucero,

- J. McClean, M. McEwen, X. Mi, M. Mohseni, J.Y. Mutus, O. Naaman, M. Neeley, M. Niu, A. Petukhov, C. Quintana, N. Rubin, D. Sank, V. Smelyanskiy, A. Vainsencher, T.C. White, Z. Yao, P. Yeh, A. Zalcman, H. Neven, and John M. Martinis. 2020. Demonstrating a continuous set of two-qubit gates for near-term quantum algorithms. *Physical Review Letters* 125, 12 (2020), 120504.
- [25] Pranav Gokhale, Ali Javadi-Abhari, Nathan Earnest, Yunong Shi, and Frederic T Chong. 2020. Optimized quantum compilation for near-term algorithms with openpulse. In *2020 53rd Annual IEEE/ACM International Symposium on Microarchitecture (MICRO)*. IEEE, 186–200.
- [26] Wenjie Gong and Soonwon Choi. 2023. Robust and parallel control of many qubits. *arXiv preprint arXiv:2312.08426* (2023).
- [27] Daniel Greenbaum. 2015. Introduction to quantum gate set tomography. *arXiv preprint arXiv:1509.02921* (2015).
- [28] K Hammerer, G Vidal, and J Ignacio Cirac. 2002. Characterization of nonlocal gates. *Physical Review A* 66, 6 (2002), 062321.
- [29] Cupjin Huang, Tenghui Wang, Feng Wu, Dawei Ding, Qi Ye, Linghang Kong, Fang Zhang, Xiaotong Ni, Zhiyun Song, Yaoyun Shi, Hui-Hai Zhao, Chunqing Deng, and Jianxin Chen. 2023. Quantum Instruction Set Design for Performance. *Physical Review Letters* 130 (Feb 2023), 070601. Issue 7. doi:10.1103/PhysRevLett.130.070601
- [30] IBM Quantum. 2024. New fractional gates reduce circuit depth for utility-scale workloads. <https://www.ibm.com/quantum/blog/fractional-gates>. Accessed: Nov. 18, 2024.
- [31] IonQ. 2023. Getting started with IonQ’s hardware-native gateset. <https://docs.ionq.com/guides/getting-started-with-native-gates>.
- [32] Justin Kalloor, Mathias Weiden, Ed Younis, John Kubiatawicz, Bert De Jong, and Costin Iancu. 2024. Quantum Hardware Roofline: Evaluating the Impact of Gate Expressivity on Quantum Processor Design. *arXiv preprint arXiv:2403.00132*.
- [33] J. Kelly, R. Barends, B. Campbell, Y. Chen, Z. Chen, B. Chiaro, A. Dunsworth, A. G. Fowler, I.-C. Hoi, E. Jeffrey, A. Megrant, J. Mutus, C. Neill, P. J. J. O’Malley, C. Quintana, P. Roushan, D. Sank, A. Vainsencher, J. Wenner, T. C. White, A. N. Cleland, and John M. Martinis. 2014. Optimal quantum control using randomized benchmarking. *Physical Review Letters* 112, 24 (2014), 240504.
- [34] Sumeet Khatri, Ryan LaRose, Alexander Poremba, Lukasz Cincio, Andrew T Sornborger, and Patrick J Coles. 2019. Quantum-assisted quantum compiling. *Quantum* 3 (2019), 140.
- [35] Youngseok Kim, Andrew Eddins, Sajant Anand, Ken Xuan Wei, Ewout Van Den Berg, Sami Rosenblatt, Hasan Nayfeh, Yantao Wu, Michael Zaletel, Kristan Temme, and William D Oliver. 2019. A quantum engineer’s guide to superconducting qubits. *Applied Physics Reviews* 6, 2 (2019), 021318.
- [36] Linghang Kong. 2021. A framework for randomized benchmarking over compact groups. *arXiv preprint arXiv:2111.10357* (2021).
- [37] Philip Krantz, Morten Kjaergaard, Fei Yan, Terry P Orlando, Simon Gustavsson, and William D Oliver. 2019. A quantum engineer’s guide to superconducting qubits. *Applied Physics Reviews* 6, 2 (2019), 021318.
- [38] Lingling Lao, Prakash Murali, Margaret Martonosi, and Dan Browne. 2021. Designing calibration and expressivity-efficient instruction sets for quantum computing. In *2021 ACM/IEEE 48th Annual International Symposium on Computer Architecture (ISCA)*. IEEE, Valencia, Spain, 846–859.
- [39] Gushu Li, Yufei Ding, and Yuan Xie. 2019. Tackling the qubit mapping problem for NISQ-era quantum devices. In *Proceedings of the twenty-fourth international conference on architectural support for programming languages and operating systems*. ACM, Providence, RI, USA, 1001–1014.
- [40] Sophia Fuhui Lin, Sara Sussman, Casey Duckering, Pranav S Mundada, Jonathan M Baker, Rohan S Kumar, Andrew A Houck, and Frederic T Chong. 2022. Let each quantum bit choose its basis gates. In *2022 55th IEEE/ACM International Symposium on Microarchitecture (MICRO)*. IEEE, 1042–1058.
- [41] Ji Liu, Alvin Gonzales, Benchen Huang, Zain Hamid Saleem, and Paul Hovland. 2025. QuCLEAR: Clifford Extraction and Absorption for Quantum Circuit Optimization. In *2025 IEEE International Symposium on High Performance Computer Architecture (HPCA)*. IEEE, 158–172.
- [42] Ji Liu, Peiyi Li, and Huiyang Zhou. 2022. Not all swaps have the same cost: A case for optimization-aware qubit routing. In *2022 IEEE International Symposium on High-Performance Computer Architecture (HPCA)*. IEEE, IEEE, Seoul, Korea, Republic of, 709–725.
- [43] Liam Madden and Andrea Simonetto. 2022. Best approximate quantum compiling problems. *ACM Transactions on Quantum Computing* 3, 2 (2022), 1–29.
- [44] Matt McEwen, Dave Bacon, and Craig Gidney. 2023. Relaxing hardware requirements for surface code circuits using time-dynamics. *Quantum* 7 (2023), 1172.
- [45] Evan McKinney, Michael Hatridge, and Alex K Jones. 2024. MIRAGE: Quantum circuit decomposition and routing collaborative design using mirror gates. In *2024 IEEE International Symposium on High-Performance Computer Architecture (HPCA)*. IEEE, IEEE, Edinburgh, United Kingdom, 704–718.
- [46] Evan McKinney, Chao Zhou, Mingkan Xia, Michael Hatridge, and Alex K Jones. 2023. Parallel driving for fast quantum computing under speed limits. In *Proceedings of the 50th Annual International Symposium on Computer Architecture*. ACM, Orlando, FL, USA, 1–13.
- [47] Yunseong Nam, Jwo-Sy Chen, Neal C. Pienti, Kenneth Wright, Conor Delaney, Dmitri Maslov, Kenneth R. Brown, Stewart Allen, Jason M. Amini, Joel Apisdorf, Kristin M. Beck, Aleksey Blinov, Vandiver Chaplin, Mika Chmielewski, Coleman Collins, Shantanu Debnath, Kai M. Hudek, Andrew M. Ducre, Matthew Keesan, Sarah M. Kreikemeier, Jonathan Mizrahi, Phil Solomon, Mike Williams, Jaime David Wong-Campos, David Moehring, Christopher Monroe, and Jungsang Kim. 2020. Ground-state energy estimation of the water molecule on a trapped-ion quantum computer. *npj Quantum Information* 6, 1 (2020), 33.
- [48] Long B Nguyen, Yosep Kim, Akel Hashim, Noah Goss, Brian Marinelli, Bibek Bhandari, Debmalya Das, Ravi K Naik, John Mark Kreikebaum, Andrew N Jordan, et al. 2024. Programmable Heisenberg interactions between Floquet qubits. *Nature Physics* 20, 2 (2024), 240–246.
- [49] Long B Nguyen, Yen-Hsiang Lin, Aaron Somoroff, Raymond Mencia, Nicholas Grabon, and Vladimir E Manucharyan. 2019. High-coherence fluxonium qubit. *Physical Review X* 9, 4 (2019), 041041.
- [50] Ahmed Omran, Harry Levine, Alexander Keesling, Giulia Semeghini, Tout T Wang, Sepehr Ebadi, Hannes Bernien, Alexander S Zibrov, Hannes Pichler, Soonwon Choi, et al. 2019. Generation and manipulation of Schrödinger cat states in Rydberg atom arrays. *Science* 365, 6453 (2019), 570–574.
- [51] Eric C Peterson, Lev S Bishop, and Ali Javadi-Abhari. 2022. Optimal synthesis into fixed xx interactions. *Quantum* 6 (2022), 696.
- [52] Eric C Peterson, Gavin E Crooks, and Robert S Smith. 2020. Fixed-depth two-qubit circuits and the monodromy polytope. *Quantum* 4 (2020), 247.
- [53] John Preskill. 2018. Quantum computing in the NISQ era and beyond. *Quantum* 2 (2018), 79.
- [54] John Preskill. 2025. Beyond NISQ: The Megaquop Machine.
- [55] Quantinuum. 2024. Native Arbitrary Angle Hardware Gates. [https://docs.quantinuum.com/systems/trainings/getting\\_started/arbitrary\\_angle\\_2\\_qubit\\_gates](https://docs.quantinuum.com/systems/trainings/getting_started/arbitrary_angle_2_qubit_gates).
- [56] Vivek V Shende, Igor L Markov, and Stephen S Bullock. 2004. Minimal universal two-qubit controlled-NOT-based circuits. *Physical Review A—Atomic, Molecular, and Optical Physics* 69, 6 (2004), 062321.
- [57] Seyon Sivarajah, Silas Dilkes, Alexander Cowtan, Will Simmons, Alec Edgington, and Ross Duncan. 2020. *t[ket]*: a retargetable compiler for NISQ devices. *Quantum Science and Technology* 6, 1 (2020), 014003.
- [58] Chao Song, Kai Xu, Hekang Li, Yu-Ran Zhang, Xu Zhang, Wuxin Liu, Qiujang Guo, Zhen Wang, Wenhui Ren, Jie Hao, et al. 2019.

- Generation of multicomponent atomic Schrödinger cat states of up to 20 qubits. *Science* 365, 6453 (2019), 574–577.
- [59] Quantum AI team and collaborators. 2020. *qsim*. doi:10.5281/zenodo.4023103
- [60] Himanshu Thapliyal and Nagarajan Ranganathan. 2009. Design of efficient reversible binary subtractors based on a new reversible gate. In *2009 IEEE Computer Society Annual Symposium on VLSI*. IEEE, IEEE, Tampa, FL, USA, 229–234.
- [61] Robert R Tucci. 2005. An introduction to Cartan’s KAK decomposition for QC programmers. arXiv preprint quant-ph/0507171.
- [62] Ken Xuan Wei, Isaac Lauer, Emily Pritchett, William Shanks, David C McKay, and Ali Javadi-Abhari. 2024. Native two-qubit gates in fixed-coupling, fixed-frequency transmons beyond cross-resonance interaction. *PRX Quantum* 5, 2 (2024), 020338.
- [63] Robert Wille, Daniel Große, Lisa Teuber, Gerhard W Dueck, and Rolf Drechsler. 2008. RevLib: An online resource for reversible functions and reversible circuits. In *38th International Symposium on Multiple Valued Logic (ismvl 2008)*. IEEE, IEEE, Dallas, TX, USA, 220–225.
- [64] K. Wright, K. M. Beck, S. Debnath, J. M. Amini, Y. Nam, N. Grzesiak, J.-S. Chen, N. C. Pienti, M. Chmielewski, C. Collins, K. M. Hudek, J. Mizrahi, J. D. Wong-Campos, S. Allen, J. Apisdorf, P. Solomon, M. Williams, A. M. Ducore, A. Blinov, S. M. Kreikemeier, V. Chaplin, M. Keesan, C. Monroe, and J. Kim. 2019. Benchmarking an 11-qubit quantum computer. *Nature communications* 10, 1 (2019), 5464.
- [65] Anbang Wu, Gushu Li, Hezi Zhang, Gian Giacomo Guerreschi, Yufei Ding, and Yuan Xie. 2022. A synthesis framework for stitching surface code with superconducting quantum devices. In *Proceedings of the 49th Annual International Symposium on Computer Architecture*. 337–350.
- [66] Christopher G Yale, Ashlyn D Burch, Matthew NH Chow, Brandon P Ruzic, Daniel S Lobser, Brian K McFarland, Melissa C Revelle, and Susan M Clark. 2025. Realization and calibration of continuously parameterized two-qubit gates on a trapped-ion quantum processor. *arXiv preprint arXiv:2504.06259* (2025).
- [67] Christopher G Yale, Rich Rines, Victory Omole, Bharath Thotakura, Ashlyn D Burch, Matthew NH Chow, Megan Ivory, Daniel Lobser, Brian K McFarland, Melissa C Revelle, et al. 2024. Noise-Aware Circuit Compilations for a Continuously Parameterized Two-Qubit Gateset. *arXiv preprint arXiv:2411.01094* (2024).
- [68] Zhaohui Yang, Dawei Ding, Chenghong Zhu, Jianxin Chen, and Yuan Xie. 2025. PHOENIX: Pauli-Based High-Level Optimization Engine for Instruction Execution on NISQ Devices. In *2025 62nd ACM/IEEE Design Automation Conference (DAC)*. 1–7. doi:10.1109/DAC63849.2025.11133028
- [69] Ed Younis, Costin C Iancu, Wim Lavrijsen, Marc Davis, and Ethan Smith. 2021. Berkeley Quantum Synthesis Toolkit (BQSKit). GitHub. doi:10.11578/dc.20210603.2
- [70] Chi Zhang, Ari B Hayes, Longfei Qiu, Yuwei Jin, Yanhao Chen, and Eddy Z Zhang. 2021. Time-optimal qubit mapping. In *Proceedings of the 26th ACM International Conference on Architectural Support for Programming Languages and Operating Systems*. 360–374.
- [71] Jun Zhang, Jiri Vala, Shankar Sastry, and K Birgitta Whaley. 2003. Geometric theory of nonlocal two-qubit operations. *Physical Review A* 67, 4 (2003), 042313.
- [72] Jun Zhang, Jiri Vala, Shankar Sastry, and K Birgitta Whaley. 2004. Minimum construction of two-qubit quantum operations. *Physical Review Letters* 93, 2 (2004), 020502.
- [73] Jun Zhang and K Birgitta Whaley. 2005. Generation of quantum logic operations from physical Hamiltonians. *Physical Review A* 71, 5 (2005), 052317.
- [74] Runshi Zhou, Fang Zhang, Linghang Kong, and Jianxin Chen. 2024. Halma: a routing-based technique for defect mitigation in quantum error correction. *arXiv preprint arXiv:2412.21000* (2024).
- [75] Alwin Zulehner and Robert Wille. 2019. Compiling SU (4) quantum circuits to IBM QX architectures. In *Proceedings of the 24th Asia and*

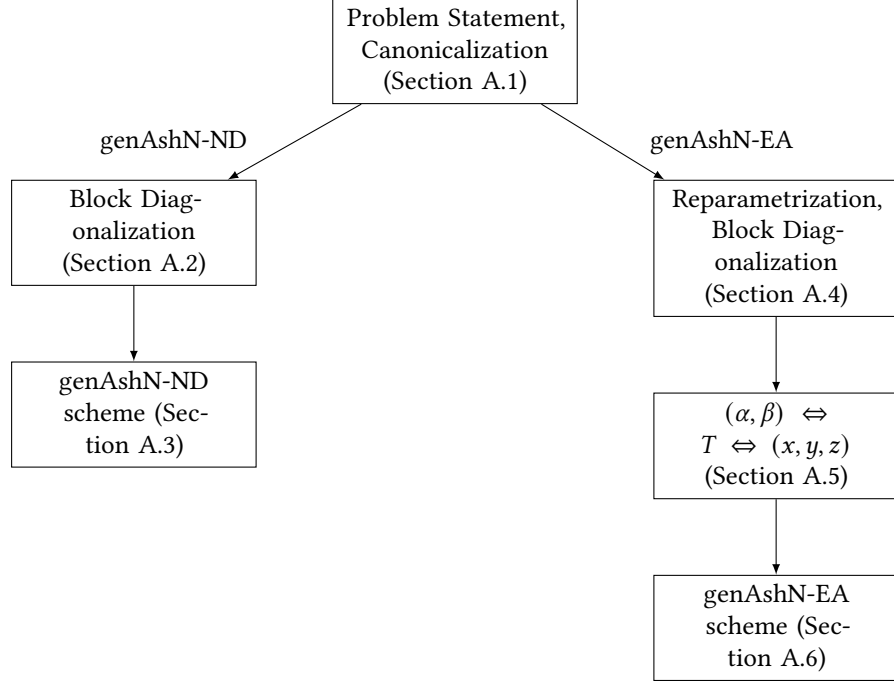


Figure 15. Overview of the proof.

## A Proof of the Algorithm 1 (genAshN gate scheme)

### Takeaways

Since the presented scheme could also be regarded as a “generalized” version of the AshN scheme and their proof and solving thoughts are sort of similar, we also call the ReQISC microarchitecture as “genAshN” scheme throughout this appendix.

### A.1 Problem Statement & Canonicalization

#### A.1.1 Hamiltonian Canonicalization. Define

$$H[a, b, c] := a \cdot \sigma_X \otimes \sigma_X + b \cdot \sigma_Y \otimes \sigma_Y + c \cdot \sigma_Z \otimes \sigma_Z.$$

We follow the canonicalization treatment in [21] and only consider two-qubit Hamiltonians of the form  $H[a, b, c]$  where  $a \geq b \geq |c|$ ,  $a > 0$ . Furthermore, we can rescale any Hamiltonian as long as the corresponding gate time is rescaled accordingly. We thus identify canonical Hamiltonian coefficients  $H[a, b, c] \sim H[ka, kb, kc]$  for all  $k > 0$ .

**A.1.2 Two-qubit gate Canonicalization.** Through the well-known canonical decomposition (or KAK decomposition) [71], any two-qubit unitary can be determined by a unique Weyl coordinate  $(x, y, z)$  such that

$$U = g \cdot (V_1 \otimes V_2) e^{i(xXX+yYY+zZZ)} (V_3 \otimes V_4), \quad g \in \{1, i\}, \quad \pi/4 \geq x \geq y \geq |z|$$

The canonical coordinate  $(x, y, z)$  which determines a class of two-qubit gates locally equivalent to the so-defined canonical gate  $\text{Can}(x, y, z) = e^{i\vec{\eta} \cdot \vec{\Sigma}} = e^{i(xXX+yYY+zZZ)}$  is confined to a tetrahedron dubbed the Weyl chamber<sup>2</sup>.

**A.1.3 Problem Statement.** Given  $H[a, b, c]$ , the minimum evolution time  $\tau_{\text{opt}}$  [28] to achieve the Weyl chamber coordinate  $(x, y, z)$ , which indicates a class of two-qubit gates locally equivalent to the so-defined canonical gate  $\text{Can}(x, y, z) = e^{-i(xXX+yYY+zZZ)}$  with  $\pi/4 \geq x \geq y \geq |z|$ , by alternately applying  $H[a, b, c]$  and single-qubit Hamiltonians  $H_0 \otimes H_1$  satisfies

<sup>2</sup>Note that for the convenience of proof, herein we select the definition of Canonical gate  $(x, y, z) \sim e^{i\vec{\eta} \cdot \vec{\Sigma}}$  that is different from the one  $(x, y, z) \sim e^{-i\vec{\eta} \cdot \vec{\Sigma}}$  in the our paper submission.



$\tau_{\text{opt}} = \min\{\tau_1, \tau_2\}$ , where

$$\begin{aligned} a\tau_1 &\geq x, \\ (a+b+c)\tau_1 &\geq x+y+z, \\ (a+b-c)\tau_1 &\geq x+y-z, \end{aligned}$$

and

$$\begin{aligned} a\tau_2 &\geq \frac{\pi}{2} - x, \\ (a+b+c)\tau_2 &\geq \frac{\pi}{2} - x + y - z, \\ (a+b-c)\tau_2 &\geq \frac{\pi}{2} - x + y + z. \end{aligned}$$

For convenience, we extend the Weyl chamber by combining it with its mirroring copy with the plane  $x = \pi/4$ . This gives us a larger tetrahedron

$$W_{\text{ext}} := \{(x, y, z) \in \mathbb{R}^3 \mid 0 \leq x \leq \pi/2, 0 \leq y \leq \min\{x, \pi/2 - x\}, -y \leq z \leq y\}.$$

It can be verified that  $W_{\text{ext}}$  is the union of the collections of the points  $(x, y, z)$  and  $(\pi/2 - x, y, -z)$  where  $(x, y, z)$  are canonical Weyl chamber coordinates satisfying  $0 \leq |z| \leq y \leq x \leq \pi/4$ . Note that  $(x, y, z) \sim (\pi/2 - x, y, -z)$  under local unitaries.

For any canonical Hamiltonian coefficients  $(a, b, c)$  and time  $\tau \geq 0$ , we define the *frontier*  $A_\tau$  to be the union of three polygons, namely

$$A_\tau := (ND(a, b, c; \tau) \cup EA_+(a, b, c; \tau) \cup EA_-(a, b, c; \tau)),$$

where

$$\begin{aligned} ND(a, b, c; \tau) &:= \{(x, y, z) \mid x = a\tau, y \pm z \in [0, (b \pm c)\tau]\}, \\ EA_+(a, b, c; \tau) &:= \{(x, y, z) \mid x + y + z = (a + b + c)\tau, a\tau \geq x \geq y \geq |z|, z \geq c\tau\}, \\ EA_-(a, b, c; \tau) &:= \{(x, y, z) \mid x + y - z = (a + b - c)\tau, a\tau \geq x \geq y \geq |z|, z \leq c\tau\}. \end{aligned}$$

For a given point  $(x, y, z) \in \mathbb{R}^3$ , we say that the frontier hits  $(x, y, z)$  at time  $\tau$  if

$$\tau = \min \left\{ t \mid (x, y, z) \in \bigcup_{t'=0}^t A_{t'} \right\}.$$

It can be verified that this is equivalent to  $\tau$  being the minimum number that simultaneously satisfies  $a\tau \geq x$ ,  $(a+b+c)\tau \geq x+y+z$  and  $(a+b-c)\tau \geq x+y-z$ , for any coordinate  $0 \leq |z| \leq y \leq x$ . This helps us formulate the optimal gate time as follows:

The optimal gate time to achieve a Weyl chamber coordinate  $(x, y, z)$  is equal to the time when the frontier hits either  $(x, y, z)$  or  $(\pi/2 - x, y, -z)$ , whichever is earlier. To prove that a gate scheme achieves optimal time, it then suffices to prove that every (extended) Weyl chamber coordinate  $(x, y, z) \in W_{\text{ext}}$  can be realized by an appropriately chosen parameter at the time the frontier hits  $(x, y, z)$ , or equivalently, every point on either of  $ND(a, b, c; \tau) \cap W_{\text{ext}}$ ,  $EA_+(a, b, c; \tau) \cap W_{\text{ext}}$  and  $EA_-(a, b, c; \tau) \cap W_{\text{ext}}$  can be realized with  $H[a, b, c]$  and local Hamiltonians within time  $\tau$ .

We prove that this is indeed the case:

**Theorem 1.** *For each Weyl chamber coordinate  $(x, y, z) \in W$  and canonical Hamiltonian coefficients  $a \geq b \geq |c|$ , let*

$$\tau_{\text{opt}}(a, b, c; x, y, z) := \min \left\{ \max \left\{ \frac{x}{a}, \frac{x+y+z}{a+b+c}, \frac{x+y-z}{a+b-c} \right\}, \max \left\{ \frac{\frac{\pi}{2}-x}{a}, \frac{\frac{\pi}{2}-x+y-z}{a+b+c}, \frac{\frac{\pi}{2}-x+y+z}{a+b-c} \right\} \right\}$$

*be the optimal time as defined above. Then, there exists  $\Omega_1, \Omega_2, \delta \in \mathbb{R}$  such that*

$$\exp\{-i\tau_{\text{opt}}(a, b, c; x, y, z)(H[a, b, c] + (\Omega_1 + \Omega_2)X \otimes I + (\Omega_1 - \Omega_2)I \otimes X + \delta(Z \otimes I + I \otimes Z))\}$$

*has Weyl chamber coordinates  $(x, y, z)$ . Moreover, at least one of  $\Omega_1, \Omega_2, \delta$  is equal to 0.*

We can prove this via a series of lemmas.

**Lemma 2** (genAshN-ND). *For any canonical Hamiltonian coefficients  $a \geq b \geq |c|$ , any  $\tau \in (0, \frac{\pi}{2a}]$ , for any Weyl chamber coordinates  $(x, y, z) \in ND(a, b, c; \tau) \cap W_{\text{ext}}$ , there exist  $r_1, r_2 \geq 0$  such that the interaction coefficients for  $U := \exp\{-i \cdot (H[a, b, c] + r_1\sigma_X \otimes I + r_2I \otimes \sigma_X) \cdot \tau\}$  are  $(x, y, z)$ .*

**Lemma 3** (genAshN-EA+). *For any canonical Hamiltonian coefficients  $a \geq b \geq |c|$ ,  $\tau \geq 0$ , for any Weyl chamber coordinates  $(x, y, z) \in EA_+(a, b, c; \tau) \cap W_{\text{ext}}$ , there exist  $\Omega, \delta \geq 0$  such that the interaction coefficients for  $U := \exp\{-i \cdot (H[a, b, c] + \Omega(\sigma_X \otimes I + I \otimes \sigma_X) + \delta(\sigma_Z \otimes I + I \otimes \sigma_Z)) \cdot \tau\}$  are  $(x, y, z)$ .*

The gate scheme for the genAshN-EA- sector can be derived from genAshN-EA+ according to the following corollary.

**Corollary 4** (genAshN-EA-). *For any canonical Hamiltonian coefficients  $a \geq b \geq |c|$ ,  $\tau \geq 0$ , for any Weyl chamber coordinates  $(x, y, z) \in EA_-(a, b, c; \tau) \cap W_{ext}$ , there exist  $\Omega, \delta \geq 0$  such that the interaction coefficients for  $U := \exp\{-i \cdot (H[a, b, c] + \Omega(\sigma_X \otimes I - I \otimes \sigma_X) + \delta(\sigma_Z \otimes I + I \otimes \sigma_Z)) \cdot \tau\}$  are  $(x, y, z)$ .*

*Proof.* For every  $(x, y, z) \in EA_-(a, b, c; \tau)$ , we want to prove that there exist  $\Omega, \delta > 0$  such that the interaction coefficients for  $U := \exp\{-i \cdot (H[a, b, c] + \Omega(\sigma_X \otimes I - I \otimes \sigma_X) + \delta(\sigma_Z \otimes I + I \otimes \sigma_Z)) \cdot \tau\}$  are  $(x, y, z)$ . We consider a similar dual problem of generating the Weyl chamber coordinates  $(x, y, -z)$  with single-qubit time-invariant Hamiltonians using  $H[a, b, -c]$ . It can be verified that  $(x, y, -z) \in EA_+(a, b, -c; \tau)$ ; therefore there exist  $\Omega'$  and  $\delta'$  such that

$$U' := \exp\{-i \cdot (H[a, b, -c] + \Omega'(\sigma_X \otimes I + I \otimes \sigma_X) + \delta'(\sigma_Z \otimes I + I \otimes \sigma_Z)) \cdot \tau\}$$

has Weyl chamber coordinates  $(x, y, -z)$ . As single-qubit gates before and after does not change the Weyl chamber coordinate, the gate

$$\begin{aligned} (\sigma_Z \otimes I)U'(\sigma_Z \otimes I) &= \exp\{-i \cdot (H[-a, -b, -c] + \Omega'(-\sigma_X \otimes I + I \otimes \sigma_X) + \delta'(\sigma_Z \otimes I + I \otimes \sigma_Z)) \cdot t\} \\ &= \exp\{-i \cdot (H[a, b, c] + \Omega'(\sigma_X \otimes I - I \otimes \sigma_X) - \delta'(\sigma_Z \otimes I + I \otimes \sigma_Z)) \cdot \tau\}^\dagger \end{aligned}$$

also has Weyl chamber coordinates  $(x, y, -z)$ . The gate

$$\exp\{-i \cdot (H[a, b, c] + \Omega'(\sigma_X \otimes I - I \otimes \sigma_X) - \delta'(\sigma_Z \otimes I + I \otimes \sigma_Z)) \cdot \tau\}$$

then has Weyl chamber coordinates  $(x, y, z)$ , indicating that  $\Omega = \Omega'$  and  $\delta = -\delta'$  suffices for the genAshN-EA- scheme.  $\square$

**A.1.4 Transforming Weyl chamber coordinates to spectrum.** The rest of the report focuses on proof of Theorem 2 and Theorem 3. Before diving into the proofs, we make a few observations that help simplify the problem to be solved.

In the case of genAshN gates, the problem of determining Weyl chamber coordinates can be mapped to determining the spectrum of a locally equivalent gate, or more specifically, gates of the form  $\exp\{-iHt\} \cdot (\sigma_Y \otimes \sigma_Y)$ .

We first state the intuition for this treatment. For all the genAshN gates, the Hamiltonians involved come from the linear subspace spanned by  $\{\sigma_X \otimes \sigma_X, \sigma_Y \otimes \sigma_Y, \sigma_Z \otimes \sigma_Z, \sigma_X \otimes I, I \otimes \sigma_X, \sigma_Z \otimes I + I \otimes \sigma_Z\}$ . It is easy to check that every element in this linear subspace is real and thus symmetric, meaning that all the genAshN gates obtained by exponentiating the genAshN Hamiltonians must be symmetric as well. For such a symmetric unitary  $U$ , its KAK decomposition should look like  $(A_1 \otimes A_2) \exp\{i\vec{\eta} \cdot \vec{\Sigma}\} (A_1 \otimes A_2)^T$ , where  $A_1, A_2 \in SU(2)$ . For a single qubit gate  $A \in SU(2)$ , one can check that  $\sigma_Y A^T \sigma_Y = A^\dagger$ . Therefore

$$\begin{aligned} U \cdot (\sigma_Y \otimes \sigma_Y) &= (A_1 \otimes A_2) (\exp\{i\vec{\eta} \cdot \vec{\Sigma}\} \cdot \sigma_Y \otimes \sigma_Y) (A_1 \otimes A_2)^\dagger \\ &\sim \exp\{i\vec{\eta} \cdot \vec{\Sigma}\} \cdot \sigma_Y \otimes \sigma_Y, \end{aligned}$$

the spectrum of which uniquely determines the Weyl chamber coordinates  $\vec{\eta}$ .

To make this rigorous, we recall the *magic basis*

$$\mathcal{M} := \frac{1}{\sqrt{2}} \begin{bmatrix} 1 & 0 & 0 & i \\ 0 & i & 1 & 0 \\ 0 & i & -1 & 0 \\ 1 & 0 & 0 & -i \end{bmatrix}.$$

The KAK decomposition can be understood under the magic basis as finding  $O_1, O_2 \in SO(4)$  such that  $\mathcal{M}^\dagger U \mathcal{M} = O_1 D O_2$  where  $D$  is a diagonal matrix containing information of the Weyl Chamber coordinates.

Going to the magic basis, for  $U = U^T$  we have

$$(\mathcal{M}^\dagger U \mathcal{M})^T = \mathcal{M}^T U \bar{\mathcal{M}}.$$

Let

$$D' = \begin{bmatrix} 1 & & & \\ & -1 & & \\ & & 1 & \\ & & & -1 \end{bmatrix}.$$

One can verify that  $\mathcal{M} D' = \bar{\mathcal{M}}$ ; therefore  $\mathcal{M}^\dagger U \mathcal{M} D' = \mathcal{M}^\dagger U \bar{\mathcal{M}}$  is a symmetric unitary, meaning that it can be diagonalized by an orthogonal matrix:

$$\mathcal{M}^\dagger U \mathcal{M} D' = O D O^T \sim D.$$

Translating this back to the computational basis, we have  $\mathcal{M} D' = (\sigma_Y \otimes \sigma_Y) \mathcal{M}$ . Thus  $U \cdot (\sigma_Y \otimes \sigma_Y) \sim D$ .

For the rest of the note, we study the two-qubit gate

$$V(a, b, c; \tau; \Omega_1, \Omega_2, \delta) \\ := \exp\{-i\tau(H[a, b, c] + \Omega_1(\sigma_X \otimes I + I \otimes \sigma_X) + \Omega_2(\sigma_X \otimes I - I \otimes \sigma_X) + \delta(\omega_Z \otimes I + I \otimes \omega_Z))\} \cdot (\sigma_Y \otimes \sigma_Y).$$

## A.2 Canonicalization for genAshN-ND

The Hamiltonian corresponding to the genAshN-ND scheme can be explicitly exponentiated. To see this more clearly, we conjugate the X- and Z-bases:

$$H_{ND} = (H \otimes H)(H[a, b, c] + \Omega_1(\sigma_X \otimes I + I \otimes \sigma_X) + \Omega_2(\sigma_X \otimes I - I \otimes \sigma_X))(H \otimes H) \\ = \begin{pmatrix} a + 2\Omega_1 & & & c - b \\ & -a + 2\Omega_2 & b + c & \\ & b + c & -a - 2\Omega_2 & \\ c - b & & & a - 2\Omega_1 \end{pmatrix}.$$

This is a  $2 + 2$  block-diagonal matrix which can be explicitly diagonalized. We then have

$$V(a, b, c; \tau; \Omega_1, \Omega_2, 0) \\ \sim (H \otimes H)V(a, b, c; \tau; \Omega_1, \Omega_2, 0)(H \otimes H) \\ = \exp\{-iH_{ND}\tau\}(\sigma_Y \otimes \sigma_Y) \\ = \begin{pmatrix} \frac{ie^{-i\tau}(c-b)\sin S_1\tau}{S_1} & & & \frac{e^{-i\tau}(-S_1\cos S_1\tau + i\Omega_1\sin S_1\tau)}{S_1} \\ & \frac{-ie^{i\tau}(b+c)\sin S_2\tau}{S_2} & \frac{e^{i\tau}(S_2\cos S_2\tau - i\Omega_2\sin S_2\tau)}{S_2} & \\ & \frac{e^{i\tau}(S_2\cos(S_2\tau) + i\Omega_2\sin S_2\tau)}{S_2} & \frac{-ie^{i\tau}(b+c)\sin S_2\tau}{S_2} & \\ e^{-i\tau}(-S_1\cos S_1\tau - i\Omega_1\sin S_1\tau) & & & \frac{ie^{-i\tau}(c-b)\sin S_1\tau}{S_1} \end{pmatrix}$$

where  $S_1 := \sqrt{4\Omega_1^2 + (b-c)^2}$ ,  $S_2 := \sqrt{4\Omega_2^2 + (b+c)^2}$ . The spectrum of  $V$  is then  $\{ie^{-i(at\pm\theta_1)}, -ie^{i(at\pm\theta_2)}\}$ , where  $\cos\theta_1 := \frac{(c-b)\sin(S_1\tau)}{S_1}$  and  $\cos\theta_2 := \frac{(b+c)\sin S_2\tau}{S_2}$ . It can be verified that such a gate corresponds to Weyl chamber coordinates  $(at, y, z)$ , where

$$\sin(y+z) = \frac{(b+c)\sin S_2\tau}{S_2}, \sin(y-z) = \frac{(b-c)\sin S_1\tau}{S_1}.$$

It suffices to prove that the polygon  $ND(t)$  can be spanned by choosing appropriate  $S_1 \geq b-c$  and  $S_2 \geq b+c$ .

## A.3 Proof of Theorem 2

*Proof.* Letting  $u = y + z$ ,  $v = y - z$ . We claim that  $u \in [0, \min\{(b+c)\tau, \pi - (b+c)\tau\}]$ . This is because

$$u = y + z \leq 2y \leq \pi - 2x = \pi - 2a\tau \leq \pi - (b+c)\tau.$$

Similarly,  $v \in [0, \min\{(b-c)\tau, \pi - (b-c)\tau\}]$ . We then only need to prove that the range of  $(b-c)\sin(S_1\tau)/S_1$  for  $S_1 \geq b-c$  covers  $[0, \sin((b-c)\tau)]$  and the range of  $(b+c)\sin(S_2\tau)/S_2$  for  $S_2 \geq b+c$  covers  $[0, \sin((b+c)\tau)]$ , both of which are obvious.  $\square$

## A.4 Canonicalization & Reparameterization for genAshN-EA

For the genAshN-EA scheme, we first rescale the Hamiltonian such that  $c = a - 1$  and denote  $\eta := a - b \in [0, 1]$ . The only case where such a canonicalization cannot be done is on the line  $a = b = c$ , but a closer inspection shows that  $EA_+(a, a, a; \tau) = \{(a\tau, a\tau, a\tau)\}$  only consists of one point, in which case Theorem 3 automatically holds for  $\Omega, \delta = 0$ . Note also that this rescaling implies  $a \geq -c = 1 - a$ , so  $a \geq \frac{1}{2}$ . Furthermore, one can show that with such a rescaling, the highest value  $\tau_{\text{opt}}$  can take over the Weyl chamber is  $\pi$ :

*Proof.* Suppose  $\tau_{\text{opt}} = \min\{\tau_1, \tau_2\} > \pi$ , i.e.  $\tau_1, \tau_2 > \pi$ . For this to happen it must be that  $(a+b+c)\tau_1 = x + y + z$  and  $(a+b+c)\tau_2 = \pi/2 - x + y - z$ , as other inequalities cannot be saturated with  $a \geq 1/2$  and  $(x, y, z) \in W_{\text{ext}}$ . However this is also impossible as it leads to

$$\pi < (a+b+c)(\tau_1 + \tau_2) = \pi/2 + 2y \leq \pi.$$

$\square$

The Hamiltonian reads

$$H_{EA} := a(\sigma_X \otimes \sigma_X + \sigma_Y \otimes \sigma_Y + \sigma_Z \otimes \sigma_Z) - \eta \cdot \sigma_Y \otimes \sigma_Y - \sigma_Z \otimes \sigma_Z + \Omega(\sigma_X \otimes I + I \otimes \sigma_X) + \delta(\sigma_Z \otimes I + I \otimes \sigma_Z).$$

We start by observing that all terms have a common eigenvector  $(0, 1, -1, 0)$ , and it is consequently an eigenvector of  $H_{EA}$  with eigenvalue  $1 + \eta - 3a$ . The other three eigenvalues are difficult to solve for explicitly, making it difficult to directly exponentiate the Hamiltonian.<sup>3</sup> We instead look at the remaining characteristic polynomial:

$$P(\lambda) := \frac{\det(H_{EA} - \lambda I)}{\lambda + 3a - 1 - \eta}.$$

$P$  is a cubic polynomial with leading coefficient  $+1$ ; moreover it can be verified that  $P(a + 1 - \eta) = -8\Omega^2 \leq 0$ , and  $P(a - 1 - \eta) = 8\delta^2 \geq 0$ . This indicates that the three real roots of  $P$  lies in  $(-\infty, a - 1 - \eta]$ ,  $[a - 1 - \eta, a + 1 - \eta]$  and  $[a + 1 - \eta, +\infty)$  respectively. Moreover, the three roots should sum up to  $3a - 1 - \eta$  as  $H_{EA}$  is traceless. We can uniquely reparameterize the eigenvalues by  $a + \eta - 1 - 2(\alpha + \beta)$ ,  $a - 1 - \eta + 2\alpha$ ,  $a + 1 - \eta + 2\beta$ , where  $\alpha \in [0, 1]$ ,  $\beta \geq 0$ ,  $\alpha + \beta \geq \eta$ . We denote the set  $Q_\eta := \{(\alpha, \beta) \in \mathbb{R}^2 | \alpha \in [0, 1], \beta \geq 0, \alpha + \beta \geq \eta\}$ . The last constraint is to ensure that  $a + \eta - 1 - 2(\alpha + \beta) \leq a - 1 - \eta$ . Inverting the parameterization by looking at the coefficients of  $P(\lambda)$  gives  $\Omega = \sqrt{(1 - \alpha)\beta(1 - \eta + \alpha + \beta)}$  and  $\delta = \sqrt{\alpha(1 + \beta)(\beta + \alpha - \eta)}$ . Since  $\Omega, \delta$  can take any non-negative value, this parameterization constitutes a bijection.

#### A.5 Correspondence between $(\alpha, \beta)$ , $T$ and $(x, y, z)$

With the above reparameterization, we know explicitly the eigenspectrum of  $H_{EA}$ . We can therefore write down the following function of the trace of

$$V(a, a - \eta, a - 1; \tau; \sqrt{(1 - \alpha)\beta(1 - \eta + \alpha + \beta)}, 0, \sqrt{\alpha(1 + \beta)(\beta + \alpha - \eta)}):$$

$$T(a, \eta; \tau, \alpha, \beta) := e^{i\tau} (\text{Tr}[V] + \exp\{-i\tau(1 + \eta - 3a)\}). \quad (5)$$

We claim that showing the range of  $T$  covers a certain set  $S \subseteq \mathbb{C}^2$  is sufficient to prove Theorem 3. To see this, we investigate the correspondence between the eigenvalue parameters  $(\alpha, \beta)$ , trace quantity  $T$  and the Weyl chamber coordinates  $(x, y, z)$ . Let us take a step back to revisit what we want to prove: We want to show that the Weyl chamber coordinates of  $V(a, a - \eta, a - 1; \tau; \Omega, 0, \delta)$  maps the pair  $(\Omega, \delta)$  surjectively onto  $EA_+(a, a - \eta, a - 1; \tau)$ . To prove this, we want to find a series of three surjective maps that compose to this particular map:

$$(\Omega, \delta) \in \mathbb{R}_{\geq 0}^2 \xrightarrow{\phi_1} (\alpha, \beta) \in Q_\eta \xrightarrow{\phi_2} T \in S \xrightarrow{\phi_3} (x, y, z) \in EA_+.$$

We have already worked out  $\phi_1$ , showing that it is a bijection. The rest of the proof focuses on finding  $\phi_2, \phi_3$  as well as the set  $S \subseteq \mathbb{C}^2$  such that surjectivity holds.

The map  $\phi_2$  is directly defined by Equation (5), but the map  $\phi_3$  is less obvious. To see why  $T$  determines the Weyl chamber coordinate  $(x, y, z)$  of  $V$ , it suffices to show that the spectrum of  $V$  can be recovered from  $T$ . Since  $V \in SU(4)$ , the four eigenvalues have the form  $-\exp\{-i\tau(1 + \eta - 3a)\}, x_1, x_2, x_3$ , where

$$\begin{cases} x_i^{-1} = \bar{x}_i, i = 1, 2, 3, \\ x_1 x_2 x_3 = -\exp\{i\tau(1 + \eta - 3a)\}, \\ x_1 + x_2 + x_3 = e^{-i\tau} T. \end{cases}$$

This indicates that  $x_1, x_2, x_3$  are the three roots of the cubic polynomial

$$\begin{aligned} & (x - x_1)(x - x_2)(x - x_3) \\ &= x^3 - (x_1 + x_2 + x_3)x^2 + (x_1 x_2 + x_1 x_3 + x_2 x_3)x - x_1 x_2 x_3 \\ &= x^3 - e^{-i\tau} T x^2 - \exp\{i\tau(1 + \eta - 3a)\}((x_3^{-1} + x_2^{-1} + x_1^{-1})x - 1) \\ &= x^3 - e^{-i\tau} T x^2 - \exp\{i\tau(1 + \eta - 3a)\}(\overline{(x_1 + x_2 + x_3)}x - 1) \\ &= x^3 - e^{-i\tau} T x^2 - \exp\{i\tau(1 + \eta - 3a)\}(e^{i\tau} \bar{T} x - 1), \end{aligned}$$

thus establishing  $\phi_3$ .

We prove the surjectivity of  $\phi_2$  and  $\phi_3$  using the following respective approaches:

- For  $\phi_2$ , we prove surjectivity using continuity: Given that the map  $\phi_2$  is continuous in a sense we will define, we take a contour  $C \subseteq Q_\eta$  in the domain and inspect its image  $\phi_2(C)$ . As the map is continuous, the image of the region enclosed by  $C$  must contain the region enclosed by  $\phi_2(C)$ , which we show contains  $S$ .

<sup>3</sup>Technically such an explicit exponentiation can be done as the remaining characteristic polynomial is only cubic. We proceed with another approach that will prove to be simpler.



- For  $\phi_3$ , we look at the fibers  $\phi_3^{-1}(x, y, z)$ . Each  $(x, y, z)$  gives rise to a finite number of choices of the spectrum of  $V$  due to different possible canonicalizations, which in turn gives rise to a finite number of  $T$ . We fix one particular canonicalization

$$(x, y, z) \mapsto (-e^{i(x+y+z)}, e^{i(x-y-z)}, -e^{i(-x+y-z)}, e^{i(-x-y+z)}),$$

such that  $\phi_3$  can be made invertible. Surjectivity is proven by verifying that  $\phi_3^{-1}(EA_+) \subseteq S$ .

## A.6 Proof of Theorem 3

**A.6.1 Continuity of  $\phi_2$ .** Let  $\gamma := 1/(1 + \beta)$  and define  $TG(\alpha, \gamma) := \phi_2(\alpha, \beta)$ . We show a stronger notion of continuity for  $\phi_2$ , that is,

$$\begin{aligned} TG = & \frac{\gamma(\alpha\gamma(\eta-1) + \alpha - \gamma\eta^2 + \gamma + \eta - 1)e^{-i\tau(-2\alpha - \frac{2}{\gamma} + \eta + 1)}}{(\gamma(\alpha - \eta - 1) + 2)(\gamma(2\alpha - \eta - 1) + 1)} + \frac{\gamma(\alpha\gamma(\alpha - \eta - 1) + \alpha + \eta - 1)e^{\frac{i\tau(\gamma\eta + \gamma - 2)}{\gamma}}}{(\alpha\gamma - 1)(\gamma(\alpha - \eta - 1) + 2)} \\ & + \frac{(\gamma(\alpha(\gamma(-\eta) + \gamma - 1) + \eta + 1) - 1)e^{i\tau(-2\alpha + \eta + 1)}}{(\alpha\gamma - 1)(\gamma(2\alpha - \eta - 1) + 1)} \end{aligned} \quad (6)$$

is continuous in the region  $U_\eta$  defined by

$$0 \leq \alpha, \gamma \leq 1 \quad (7)$$

$$\gamma(\alpha - 1) + 1 \geq \eta\gamma. \quad (8)$$

This shows that  $\phi_2$  is not only continuous in the interior of  $Q_\eta$ , it is continuous at the boundary as well, especially when  $\beta \rightarrow \infty$ . This allows us to take a contour with  $\beta \rightarrow \infty$ .

Now according to the expression for  $TG$  in eq. (6), we can only have problems with continuity if one or more of the following equations hold:

$$\begin{aligned} \gamma(\alpha - \eta - 1) + 2 &= 0 \\ \gamma(2\alpha - \eta - 1) + 1 &= 0 \\ \alpha\gamma - 1 &= 0. \end{aligned}$$

When  $\gamma = 0$ , none of these equations can be satisfied. When  $\gamma > 0$ , the equations can be translated to

$$\begin{aligned} \alpha + 2/\gamma - 1 &= \eta \\ 2\alpha + 1/\gamma - 1 &= \eta \\ \alpha &= 1/\gamma. \end{aligned}$$

Since  $1/\gamma > 0$ , the first equality is never satisfied because of eq. (8). Assume  $0 < \alpha < 1$ . Then, the second equality is never satisfied due to eq. (8). Furthermore, the third equality is never satisfied since  $1/\gamma \in [1, \infty)$ . The only two limits we need to compute are therefore

$$\begin{aligned} \alpha \rightarrow 0, \gamma &\rightarrow 1/(1 + \eta) \\ \alpha \rightarrow 1, \gamma &\rightarrow 1 \end{aligned}$$

given  $\gamma > 0$ . We compute the first limit. Let  $\epsilon > 0$  and  $h \in \mathbb{R}$  be small. We can show

$$\begin{aligned} TG|_{\alpha=\epsilon, \gamma=1/(1+\eta)+h} &= e^{i\tau(1+\eta)} \frac{2(\eta+1)(\eta(h-1)+h)}{(\eta+(1+\eta)h(-\eta+\epsilon-1)+\epsilon+1)(-\eta+\epsilon(\eta h+h+1)-1)} \\ &+ e^{-i\tau(1+\eta)} O(1) + O(\epsilon+h). \end{aligned}$$

Next, we compute the second limit. Let  $\epsilon, \epsilon' > 0$ . We can show

$$\begin{aligned} TG|_{\alpha=1-\epsilon, \gamma=1-\epsilon'} &= -e^{-i\tau(-4+\eta+1)} \frac{(\epsilon'-1)((\eta-1)(\eta+\epsilon)\epsilon' - \eta(\eta+\epsilon-2))}{(-\eta+(\eta+\epsilon)\epsilon' - \epsilon+2)(-\eta+(\eta+2\epsilon-1)\epsilon' - 2\epsilon+2)} \\ &+ e^{-i\tau(1-\eta)} \frac{2(-\eta+(\eta+\epsilon-1)\epsilon' - \epsilon+2)(-\eta+(\eta+\epsilon)\epsilon' - \epsilon+1)}{(-\eta+(\eta+\epsilon)\epsilon' - \epsilon+2)(-\eta+(\eta+2\epsilon-1)\epsilon' - 2\epsilon+2)} + O(\epsilon+h). \end{aligned}$$

Since  $\eta \in [0, 1]$ , the denominators for both of these expressions do not vanish as  $\epsilon, h, \epsilon' \rightarrow 0$ . Thus,  $TG$  converges to its corresponding value throughout  $U_\eta$  and is thus continuous on  $U_\eta$ .

**A.6.2 Surjectivity of  $\phi_2$ .** When  $\alpha, \gamma$  traverses along the boundary of  $U_\eta$ , we claim  $TG$  encloses  $S$ , a region of the complex plane enclosed by the arc around the unit circle from  $D := e^{i(\eta-1)\tau}$  to  $C := e^{i(\eta+1)\tau}$  by increasing the complex argument by  $2\tau$ , denoted  $\widehat{DC}$  and the two line segments  $\overline{AC}$  and  $\overline{AD}$ , where  $A := e^{i\tau(\eta-1)} + e^{i\tau(\eta+1)} - e^{i\tau(1-\eta)}$ . This defines the boundary of  $S$ . For clarity we will explicitly define the interior of  $S$ . We can do this by splitting into cases:

1. If  $2\tau = 0$ ,  $A = C = D$  and  $S := \{1\}$ .
2. If  $0 < 2\tau < 2\pi$ , we can show that each line segment can only intersect  $\widehat{DC}$  once: For any point  $E$ , the line segment  $\overline{CE}$  intersects with  $\widehat{DC}$  only if the angle of  $\overline{CE}$  lies strictly within the angle of  $\widehat{DC}$  and the angle of the tangent line at  $C$ , that is,  $[\eta\tau - \pi/2, (\eta+1)\tau - \pi/2]$ . We have  $\overline{CA} = -2i \sin((1-\eta)\tau)$  and the angle is  $-\pi/2$ , which is not strictly in this range. A similar argument applies to the point  $D$ , where the range is  $[(\eta-1)\tau + \pi/2, \eta\tau + \pi/2]$  and the angle of  $\overline{DA}$  is  $\tau + \pi/2$ . Thus, the intersection of  $\triangle ADC$  with the segment of the circle corresponding to  $\widehat{DC}$  is exactly  $\overline{DC}$ . We then define  $S$  as the region enclosed by  $\triangle ADC$  but with  $\overline{DC}$  replaced by  $\widehat{DC}$ .
3. If  $2\tau = 2\pi$ ,  $C = D$  and we define  $S = \overline{CA} \cup \overline{D^1}$ , where  $\overline{D^1}$  is the closed unit disk.

Now, we compute the value of  $TG$  at the edges:

$$\begin{aligned}
 TG|_{\alpha=0} &= \frac{e^{\frac{i\tau(\gamma\eta+\gamma-2)}{\gamma}} \left( \gamma(\eta-1) \left( -e^{-\frac{2i\tau(\gamma\eta+\gamma-2)}{\gamma}} \right) + (\gamma\eta + \gamma - 2)e^{\frac{2i\tau}{\gamma}} + \gamma(\eta-1) \right)}{\gamma\eta + \gamma - 2}, \\
 TG|_{\alpha=1} &= \frac{e^{-\frac{i\tau(\gamma(\eta-1)-2)}{\gamma}} \left( \gamma\eta e^{\frac{2i\tau(\gamma\eta-2)}{\gamma}} + (\gamma\eta - 2)e^{\frac{2i\tau(\gamma(\eta-1)-1)}{\gamma}} - \gamma\eta \right)}{\gamma\eta - 2}, \\
 TG|_{\gamma=1} &= -\frac{e^{i(\eta-1)\tau} \left( 2\alpha + \eta \left( e^{2i\tau(\alpha-\eta+1)} - e^{-2i(\alpha-1)\tau} - 1 \right) \right)}{\eta - 2\alpha}, \\
 TG|_{\gamma=0} &= e^{i\tau(-2\alpha+\eta+1)}, \\
 TG|_{\alpha=-1/\gamma+1+\eta} &= \frac{e^{\frac{i\tau(\gamma\eta+\gamma-2)}{\gamma}} \left( \gamma(\eta-1) \left( -e^{-\frac{2i\tau(\gamma\eta+\gamma-2)}{\gamma}} \right) + (\gamma\eta + \gamma - 2)e^{\frac{2i\tau}{\gamma}} + \gamma(\eta-1) \right)}{\gamma\eta + \gamma - 2}.
 \end{aligned}$$

We consider the contour  $(\eta, 1) - (0, 1/(1+\eta)) - (0, 0) - (1, 0) - (1, 1) - (\eta, 1)$  around  $U_\eta$ . We compute

$$\begin{aligned}
 TG|_{(\alpha,\gamma)=(\eta,1)} &= e^{i\tau(\eta-1)} + e^{i\tau(\eta+1)} - e^{i\tau(1-\eta)} = A \\
 B := TG|_{(\alpha,\gamma)=(0,1/(1+\eta))} &= e^{-i\tau(1+\eta)} \frac{1-\eta}{1+\eta} + e^{i\tau(1+\eta)} \frac{2\eta}{1+\eta} \\
 TG|_{(\alpha,\gamma)=(0,0)} &= e^{i\tau(\eta+1)} = C \\
 TG|_{(\alpha,\gamma)=(1,0)} &= e^{i\tau(\eta-1)} = D \\
 E := TG|_{(\alpha,\gamma)=(1,1)} &= e^{i\tau(\eta-1)} 2 \frac{1-\eta}{2-\eta} + e^{-i\tau(\eta-3)} \frac{\eta}{2-\eta}
 \end{aligned}$$

We claim the image of the contour contains the boundary of  $S$ . In particular,  $A, B, C$  and  $A, E, D$  each lie on a straight line. First, we expand the expression for  $TG$  when  $\alpha = 0$ :

$$\begin{aligned}
 TG|_{\alpha=0} &= -e^{-i\tau(\eta+1-2/\gamma)} \frac{\gamma(\eta-1)}{\gamma(\eta+1)-2} + e^{i\tau(\eta+1)} + e^{i\tau(\eta+1-2/\gamma)} \frac{\gamma(\eta-1)}{\gamma(\eta+1)-2} \\
 &= e^{i\tau(\eta+1)} + 2(\eta-1) \frac{\sin[\tau(\eta+1-2/\gamma)]}{\eta+1-2/\gamma} \times i,
 \end{aligned}$$

where we take  $\gamma > 0$  to simplify the expression (We already know by continuity that it goes to the desired value when  $\gamma \rightarrow 0$ ). Hence, in this case  $TG$  lies on a vertical line and contains  $C$  and  $B$  when we vary  $\gamma \in [0, 1/(1+\eta)]$ . Thus by continuity it must contain  $\overline{BC}$ . Furthermore,  $TG|_{\alpha=-1/\gamma+1+\eta}$  has the same expression, and thus it lies on a vertical line and contains  $B$  and  $A$  when we vary  $\gamma \in [1/(1+\eta), 1]$ . Thus, it contains  $\overline{AB}$ . Next, we expand the expression for  $\gamma = 1$ :

$$TG|_{\gamma=1} = e^{i\tau(\eta-1)} + \frac{2\eta}{\eta-2\alpha} \sin[\tau(\eta-2\alpha)] \times ie^{i\tau}.$$

Thus, if we vary  $\alpha \in [\eta, 1]$ , we lie on a line segment that contains  $A$  and  $E$  and thus by continuity contains the line segment  $\overline{EA}$ . We next consider  $\alpha = 1$ :

$$TG|_{\alpha=1} = e^{i\tau(\eta-1)} + \frac{2\gamma\eta}{\gamma\eta-2} \sin[\tau(\eta-2/\gamma)] \times ie^{i\tau},$$

where again we take  $\gamma > 0$ . This is again a straight line segment and contains  $E$  and  $D$  as we vary  $\gamma \in [0, 1]$ . Hence, it contains the line segment  $\overline{DE}$ . Furthermore, we see that for both  $\gamma = 1$  and  $\alpha = 1$ ,  $TG$  takes the form

$$e^{i\tau(\eta-1)} + rie^{i\tau},$$

for some variable  $r \in \mathbb{R}$  and thus  $\overline{EA}$  and  $\overline{DE}$  lie on the same line. Finally, from the expression for  $\gamma = 0$ ,  $TG$  moves from  $D$  to  $C$  spanning angle  $2\tau$  as we range  $\alpha$  from 1 to 0. The claim thus follows.

Since  $\phi_2$  is continuous, it maps a compact set  $U_\eta$  in  $\mathbb{R}^2$  to a compact set in  $\mathbb{C}$ . We consider the following cases

1.  $2\tau = 0$ . Then  $S$  is simply  $\{1\}$  and  $\gamma = 0$  is sufficient to achieve this point.
2. When  $0 < 2\tau < 2\pi$ ,  $\phi_2(\partial U_\eta)$  is the boundary of a triangle with one of edges replaced by an arc. Thus, it is clear  $S$  is the only compact set with boundary  $\phi_2(\partial U_\eta)$ .
3. When  $2\tau = 2\pi$ ,  $\phi_2(\partial U_\eta) = \overline{CA} \cup S^1$ , where  $S^1$  is the unit circle. It is clear the only compact set with this boundary is  $S = \overline{CA} \cup \overline{D^1}$ .

Hence  $\phi_2$  is surjective.

**A.6.3 Surjectivity of  $\phi_3$ .** Now, we know  $\tau \in [0, \pi]$ . We claim that the image of the Weyl chamber region  $W \supseteq EA_+$  defined as the polygon  $PQRM$ , where

$$\begin{aligned} P &:= (a\tau, (a-\eta)\tau, (a-1)\tau), \\ Q &:= (a\tau, (a-(1+\eta)/2)\tau, (a-(1+\eta)/2)\tau), \\ R &:= ((a-(1+\eta)/3)\tau, (a-(1+\eta)/3)\tau, (a-(1+\eta)/3)\tau), \\ M &:= ((a-\eta/2)\tau, (a-\eta/2)\tau, (a-1)\tau), \end{aligned}$$

via  $\phi_3^{-1}$  (with respect to our fixed canonicalization) is exactly  $S$ . Now,  $\phi_3^{-1}$  maps a coordinate  $(x, y, z)$  in the Weyl chamber to the complex number

$$e^{i\tau a} (e^{i(x-y-z)} - e^{i(-x+y-z)} + e^{i(-x-y+z)}). \quad (9)$$

Thus,

$$\begin{aligned} \phi_3^{-1} : P &\mapsto e^{i\tau(\eta+1)} - e^{i\tau(1-\eta)} + e^{i\tau(\eta-1)} = A \\ Q &\mapsto e^{i\tau(\eta+1)} - 1 + 1 = e^{i\tau(\eta+1)} = C \\ R &\mapsto e^{i\tau(\eta+1)/3} \\ M &\mapsto e^{i\tau} - e^{i\tau} + e^{i\tau(\eta-1)} = e^{i\tau(\eta-1)} = D. \end{aligned}$$

We consider the image of  $\overline{PQ}$  parameterized by  $(a\tau, (a-\eta+t(\eta-1)/2)\tau, (a-1-t(\eta-1)/2)\tau)$ ,  $t \in [0, 1]$ :

$$\begin{aligned} &e^{i\tau(\eta-t(\eta-1)/2+1+t(\eta-1)/2)} - e^{i\tau(-\eta+t(\eta-1)/2+1+t(\eta-1)/2)} + e^{i\tau(\eta-t(\eta-1)/2-1-t(\eta-1)/2)} \\ &= e^{i\tau(\eta+1)} - e^{i\tau(t-1)(\eta-1)} + e^{-i\tau(t-1)(\eta-1)} \\ &= e^{i\tau(\eta+1)} - 2i \sin[\tau(t-1)(\eta-1)]. \end{aligned}$$

This is clearly  $\overline{AC}$  since  $\tau \in [0, \pi]$  and so the second term cannot change sign. We next consider the image of  $\overline{PM}$ , parameterized by  $((a-t\eta/2)\tau, (a-\eta+t\eta/2)\tau, (a-1)\tau)$ ,  $t \in [0, 1]$ :

$$\begin{aligned} &e^{i\tau(-t\eta/2+\eta-t\eta/2+1)} - e^{i\tau(t\eta/2-\eta+t\eta/2+1)} + e^{i\tau(t\eta/2+\eta-t\eta/2-1)} \\ &= e^{i\tau(\eta+1-t\eta)} - e^{i\tau(1-\eta+t\eta)} + e^{i\tau(\eta-1)} \\ &= e^{i\tau(\eta-1)} + 2 \sin[\tau\eta(1-t)] \times ie^{i\tau}. \end{aligned}$$

This is clearly  $\overline{AD}$ . We next look at the image of  $\overline{QR}$ , parameterized by  $((a-t(1+\eta)/3)\tau, (a-(1+\eta)/2+t(1+\eta)/6)\tau, (a-(1+\eta)/2+t(1+\eta)/6)\tau)$ ,  $t \in [0, 1]$ :

$$e^{i\tau(-2t(1+\eta)/3+(1+\eta))} - e^{i\tau(t(1+\eta)/3)} + e^{i\tau(t(1+\eta)/3)} = e^{i\tau(-2t(1+\eta)/3+(1+\eta))}.$$

We also look at the image of  $\overline{RM}$ , parameterized by  $((a - (1 + \eta)/3 + t(2 - \eta)/6)\tau, (a - (1 + \eta)/3 + t(2 - \eta)/6)\tau, (a - (1 + \eta)/3 - t(2 - \eta)/3)\tau)$ ,  $t \in [0, 1]$ :

$$e^{i\tau((1+\eta)/3+t(2-\eta)/3)} - e^{i\tau((1+\eta)/3+t(2-\eta)/3)} + e^{i\tau((1+\eta)/3-2t(2-\eta)/3)} = e^{i\tau((1+\eta)/3-2t(2-\eta)/3)}.$$

Hence, we can see explicitly that this traces out  $\widehat{DC}$ . Therefore  $\partial W \mapsto \partial S$ . Now,  $W$  is a compact set in  $\mathbb{R}^3$ . Since eq. (9) is continuous, the image of  $W$  is a compact set in  $\mathbb{C}$ . The rest of the argument is similar to that of section A.6.2. The claim thus follows.